

https://dspace.org/

Ambient noise surfacewave imaging in a hardrock environment implications for mineral exploration

Z Wilczynski; A Kaslilar; A Malehmir; Musa Manzi; L Vivin ...

https://hdl.handle.net/10539/46412
WOS

Downloaded from a DSpace repository. https://dspace.org/

Geophysical Journal International

Geophys. J. Int. (2025) **240,** 571–590
Advance Access publication 2024 November 04
GJI Applied and Marine Geophysics

https://doi.org/10.1093/gji/ggae392

Ambient noise surface-wave imaging in a hardrock environment: implications for mineral exploration

Zbigniew Wilczynski [1], Ayse Kaslilar [1], Alireza Malehmir,[1] Musa Manzi,[2] Lilas Vivin,[3] Jean Lepine,[3] Oleg Valishin[3] and Karin Högdahl[1]

[1] *Department of Earth Sciences, Uppsala University, 75236 Uppsala, Sweden.*
E-mails: zbigniew.wilczynski@geo.uu.se (ZW); ayse.kaslilar@geo.uu.se (AK); alireza.malehmir@geo.uu.se (AM)
[2] *School of Geosciences, University of the Witwatersrand, 2050 Johannesburg, South Africa*
[3] *Sercel, 44470 Carquefou, France*

Accepted 2024 October 30. Received 2024 September 29; in original form 2024 June 19

SUMMARY

The advancement of seismic methods is vital for mineral exploration in the ongoing energy transition. In this study, we investigate the application of ambient noise seismic interferometry and surface-wave analysis to characterize the subsurface in a mineral exploration context. We then confirm the results of the passive seismic investigation through an active source experiment. We collected ambient noise data using a 2-D seismic line initially deployed for an active source reflection seismic study. By cross-correlating the signals, we retrieved the surface waves and constructed a 2-D shear-wave velocity profile using conventional surface-wave analysis. We utilized the active source data to establish initial assumptions about the surveyed medium and then validated the passive seismic experiment. The passive seismic results are concordant with the active source results and allow for the interpretation of geological contacts and fault zones. Our work demonstrates the potential of passive seismic methods for investigating local tectonic settings and their role in hardrock mineral exploration.

Key words: Seismic interferometry; Seismic noise; Surface waves and free oscillations.

1 INTRODUCTION

Improved mineral exploration has been indicated as one of the key factors in reaching the United Nations' sustainable development goals and the Paris Agreement (Ali *et al.* 2017). Geophysical prospecting plays a crucial role in mineral exploration. In particular, the seismic methods offer distinct advantages in high-resolution depth-targeting (Eaton *et al.* 2003). However, seismic exploration in a hardrock environment, fundamentally related to mineral exploration, yields specific complications, such as low acoustic impedance contrasts, low signal-to-noise ratio, and strong medium metamorphism and deformation (Salisbury *et al.* 2003). Moreover, the propagating surface waves tend to have higher frequencies (Malehmir *et al.* 2012) and lower amplitudes (Pileggi *et al.* 2011) compared to sedimentary environments. The advancements in seismic mineral exploration are thus necessary to overcome the hardrock constraints and to extend the depths and resolution of geophysical prospecting (Malehmir *et al.* 2012). In particular, passive seismic exploration using ambient seismic noise is gaining more attention due to its versatility and reduced costs (Alcalde *et al.* 2022).

Seismic interferometry (SI) and Green's function retrieval encompass studies of interference between pairs of seismic signals, reconstructing the information about the waves propagating through the interstation medium or providing information about the medium itself. Originating from the work of Claerbout (1968), SI went through a series of developments (Curtis *et al.* 2006, and references therein). Both theoretical studies and field examples validate the estimation of Green's function from cross-correlation of diffuse wavefields (Campillo & Paul 2003; Wapenaar 2004; Roux *et al.* 2005; Snieder *et al.* 2006) with applications in the exploration setting (e.g. Draganov *et al.* 2007; Halliday *et al.* 2008; Snieder & Wapenaar 2010; Draganov *et al.* 2013; Chamarczuk *et al.* 2022). Surface waves, being the most energetic part of the seismic wavefield, offer advantages in the interferometric reconstruction of the Green's function (Halliday & Curtis 2008) and thus have been primarily used in ambient noise seismic interferometry (ANSI) studies. The studies of Shapiro *et al.* (2005), Yao *et al.* (2006), Gerstoft *et al.* (2006), and Bensen *et al.* (2007), provide canonical examples of processing passive records to retrieve surface waves from cross-correlations.

The applications of surface-wave analysis for the shallow subsurface characterization are well-documented, for example in review papers and practitioners guides (Socco & Strobbia 2004; Socco *et al.* 2010; Foti *et al.* 2014; dal Moro 2015; Foti *et al.* 2018), with many available open-source tools (e.g. Wathelet *et al.* 2020). A significant development in the field was the presentation of the multichannel analysis of surface waves (MASW) method by Park *et al.* (1999). Followed by further developments (e.g. Xia *et al.* 2002; Park *et al.*

© The Author(s) 2024. Published by Oxford University Press on behalf of The Royal Astronomical Society. This is an Open Access article distributed under the terms of the Creative Commons Attribution License (https://creativecommons.org/licenses/by/4.0/), which permits unrestricted reuse, distribution, and reproduction in any medium, provided the original work is properly cited.

Downloaded from https://academic.oup.com/gji/article/240/1/571/7875257 by Witwatersrand Health Sciences Library user on 08 August 2025

2007; Park & Miller 2008), MASW became the most common active source surface-wave analysis method (Foti *et al.* 2018), using a refraction-like seismic array with an energy source at the beginning of the line.

The use of linear arrays was further expanded with ambient noise studies. Louie (2001) and Strobbia & Cassiani (2011) explored applications of ambient noise in a linear array using the refraction microtremor method (ReMi). Other authors (e.g. Park *et al.* 2007; McBride *et al.* 2019) reported the benefit of complementing active-source study by ANSI to extend the depth of investigation and aid the identification of surface-wave modes. Cheng *et al.* (2016) and Deng *et al.* (2022) suggested other 2-D geometry applications using ambient seismic noise. The use of linear arrays for ambient noise seismic interferometry was criticized due to its sensitivity to noise directionality bias and incorrect velocity estimation (Park *et al.* 2007; Foti *et al.* 2018; Zhang *et al.* 2022). Cheng *et al.* (2023) provided an extensive overview of the possible linear-array artefacts. However, authors (e.g. Cheng *et al.* 2015; Le Feuvre *et al.* 2015; Pan *et al.* 2016) present successful applications of linear arrays for ambient noise surface-wave analysis using the virtual shot gathers (following Bakulin & Calvert 2006; Snieder *et al.* 2006).

The surface-wave methods for near-surface applications are primarily employed in soft-rock (sedimentary) environments and rely on the assumptions of a dispersive layered-earth model (Park *et al.* 1999, 2007; dal Moro 2015; Foti *et al.* 2014, 2018). However, in hardrock exploration, these assumptions can be challenged due to the absence of a soft layer, the presence of a non-dispersive crystalline basement, or a complex medium with sharp lateral boundaries.

Surface-wave phase velocities are higher on stiff sites, resulting in longer wavelengths and extending the investigation depth. Yet, recording long wavelengths requires relatively long arrays, which impedes lateral resolution. Furthermore, the surface-wave generation and propagation mechanism at stiff sites is less efficient (Foti *et al.* 2018), and the signal dominant frequency and energy depend on the presence and thickness of a soft overburden (Pileggi *et al.* 2011).

There are several documented applications of surface-wave studies in the context of mineral exploration. The active source studies aim at augmenting reflection seismic surveys (Balestrini *et al.* 2019; Papadopoulou *et al.* 2019, 2023), tunnel and void detection (Sherman *et al.* 2014; Rector *et al.* 2015; Ivanov *et al.* 2016), or performing a surface-wave tomography using 3-D arrays (Rector *et al.* 2015; Da Col *et al.* 2019). Colombero *et al.* (2022) provided an example of combining passive and active experiments for surface-wave tomography in a phosphorus mine. Other authors obtained tomographic images using only ambient vibrations recorded with 3-D arrays in various mining settings (Chen *et al.* 2021; Liu *et al.* 2022; Ryberg *et al.* 2022; Zheng *et al.* 2022; Li *et al.* 2023; Olivier *et al.* 2024). The use of ambient noise with linear receiver arrays in mineral exploration settings is not common. Some notable examples include a study by Wang *et al.* (2022), who used ambient noise recorded with a linear array to locate voids, and Deng *et al.* (2022), who introduced the extended phase-shift method for linear arrays to characterize deep ore deposits.

This work presents a field study on ambient noise recorded using a linear array (Fig. 1a) set out primarily for active source reflection seismic imaging for mineral exploration. We use a conventional processing scheme based on well-known ambient noise and surface-wave analysis techniques. As proposed by Yao *et al.* (2006), we retrieve the medium's response using cross-correlation for ANSI. Then, we use the Geopsy open-source tool (Wathelet *et al.* 2020) to extract dispersion curves (DCs) from virtual common midpoint gathers. Capitalizing on the low-frequency content of the ambient noise, we reach depths of investigation of several hundred meters and provide a geological interpretation of the identified shear-wave velocity distribution. Supporting our investigation with the active source seismic experiment and available geodata, we show the potential of incorporating ambient noise studies in mineral exploration as a link between deep-targeting seismic reflection studies and shallow active source surface-wave experiments, leading to an improved understanding of the complex hardrock geology of the area.

2 EXPERIMENTAL SITE

Blötberget iron oxide apatite deposit is located in the Bergslagen ore province in central Sweden – a major mining district in Sweden and Europe. Iron oxide deposits in this region occur in three primary forms: banded iron formation, iron oxide skarn mineralization and iron oxide apatite mineralization (Ripa & Kübler 2003). Additionally, Bergslagen is recognized as a promising area for rare earth element exploration (Goodenough *et al.* 2016).

The primary lithologies in Bergslagen were formed during the Paleoproterozoic between 1.9 and 1.8 Ga, during the Svecokarelian orogeny (Stephens 2009). At the waning stage of the ca. 1.9 Ga volcanic activity, calc-alkaline and mostly felsic volcanic siltstones and sandstones were formed. They are intercalated with carbonate rocks and accompanied by thermal subsidence and penecontemporaneous granitoids. These lithologies underwent polyphase deformation and low-pressure regional metamorphism (Stephens 2009), and the supracrustal units occur as inliers in the intrusive rocks (Allen *et al.* 1996). Granites and associated pegmatites represent younger Paleoproterozoic rocks.

Skarn deposits are the most common mineralization type in Bergslagen (Magnusson 1970) formed by a reaction between carbonate beds and syn-magmatic silica and metal-rich hydrothermal fluids (Allen *et al.* 1996). Other, less common types of mineralization include banded iron formations and iron oxide apatite deposits. The latter, found only in the western part of Bergslagen, are Kiruna-type deposits (Jonsson *et al.* 2013; Högdahl *et al.* 2020) oriented conformably to the bedding of the metavolcanic host rock (Magnusson 1970).

The older bedrock in the Blötberget area (Fig. 1b) comprises felsic metavolcanic rocks of rhyolitic to rhyodacitic composition and metagranitoids (SGU 2022). They have an NE strike and a foliation that dips between 60 and 80 degrees to SE (Högdahl et al. 2020). A younger granitic intrusion is located ca. 3.5 km southeast of Blötberget. An NE–SW striking fault is identified close to the contact of metavolcanic rocks and the metagranitoid (e.g. Magnusson 1970; SGU 1988), supported by a topographic lineament (Fig. 1a).

The iron oxide apatite deposit at Blötberget occurs as a sheet-like body hosted by metavolcanic rocks (Nordic Iron Ore 2011). It is moderately dipping towards the southeast (Markovic *et al.* 2019; Högdahl *et al.* 2020), with a thickness of up to 30 m (Malehmir *et al.* 2017), and reaching a depth of 1200 m (Malehmir *et al.* 2021). The NE strike of the mineralization is shown with marked old mines and mineral prospects on the geological map (Fig. 1b). In an adjacent metavolcanic inlier to the southeast, there are a series of other mines and mineral prospects that extend towards north-east to thin, variably mineralized skarn layers, following a magnetic anomaly in the airborne magnetic map (Fig. 1c). Kiruna-type and skarn deposits in this area were described by Geijer & Magnusson (1944).

Downloaded from https://academic.oup.com/gji/article/240/1/571/7875257 by Witwatersrand Health Sciences Library user on 08 August 2025

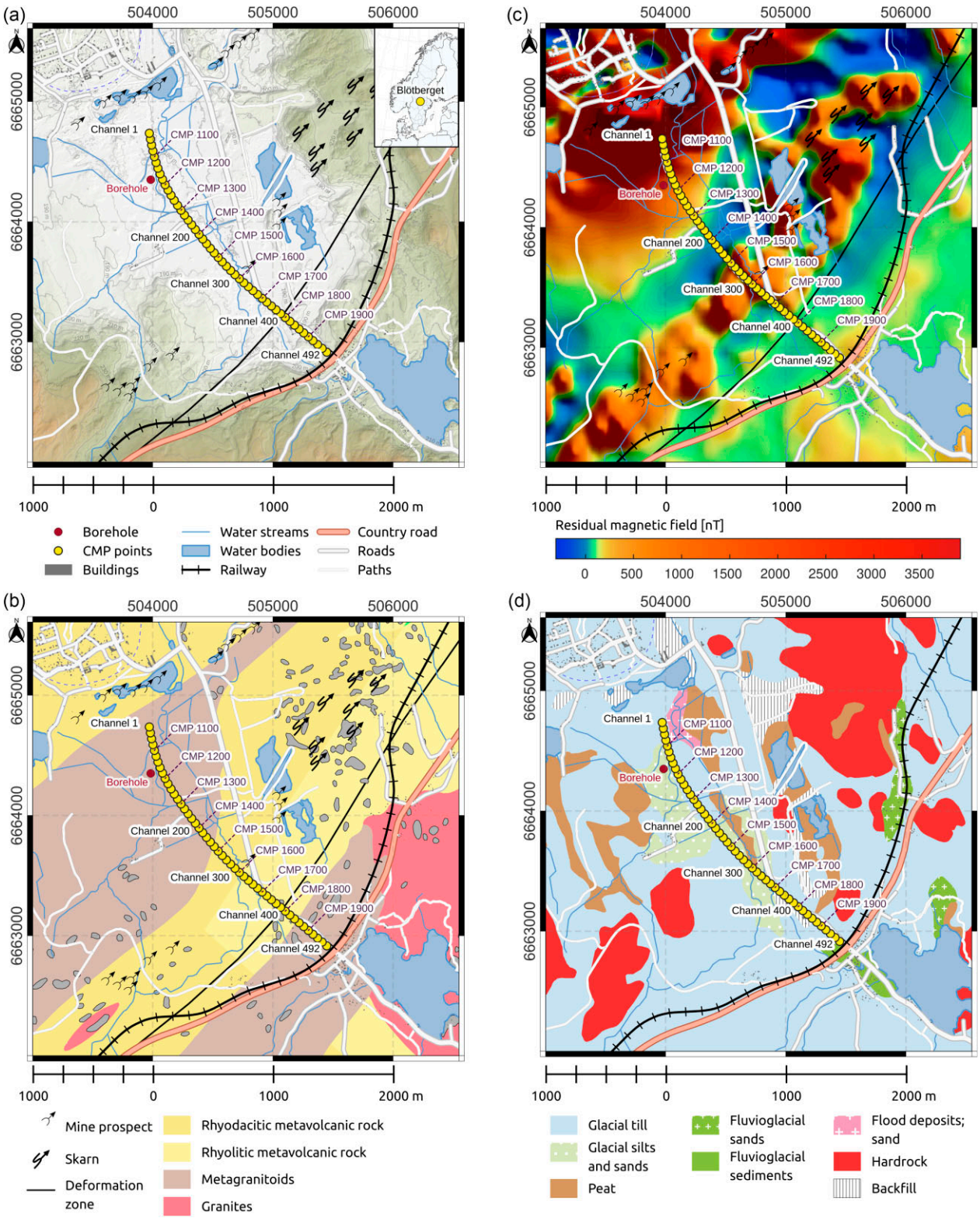


Figure 1. Maps presenting profile channels and common midpoints (CMP) with available geodata. (a) Topography map with elevation profile. (b) Bedrock geology map, modified from Geological Survey of Sweden (SGU, 1988, 2018a). (c) Airborne residual magnetic anomaly map with mineral prospects locations. (d) Soil type map, modified from SGU (2018b).

Downloaded from https://academic.oup.com/gji/article/240/1/571/7875257 by Witwatersrand Health Sciences Library user on 08 August 2025

This work is part of a long-term exploration initiative in Blötberget taking place due to the recently regained interest in mineral exploration. The industry reports contain valuable information from the formerly operating mine (closed in the 1970s) and the mining company currently considering reopening the mine (Nordic Iron Ore 2011). Additionally, the site has served as a geophysical test site for over a decade, allowing for developing innovative solutions and characterization of the subsurface (Malehmir *et al.* 2020, 2023, and references therein). The extensive geophysical investigations have led to the petrophysical and volumetric characterization of the deep iron-oxide deposit (e.g. Maries *et al.* 2017; Malehmir *et al.* 2021) and the identification of other deep reflectors interpreted as mineralization (Markovic *et al.* 2019; Pertuz *et al.* 2021). Several surface-wave studies in the area have focused on improving reflection seismic imaging (Balestrini *et al.* 2019; Papadopoulou *et al.* 2023) and characterizing the subsurface down to approximately 100 m (Papadopoulou *et al.* 2019, 2021). However, up to date, no seismic experiment on this site has focused on the moderate-scale depths of several hundred meters.

The most recent field campaign took place in 2022 June. It comprised the acquisition of drone-based magnetic and electromagnetic data, surface fibre optic distributed acoustic sensing (DAS) data, borehole helically wound cable DAS data, and conventional active source seismic data using 150 3-component geophones and almost 500 vertical component accelerometers. The studies so far have shown a potential of broadband data for mineralization delineation (Gyger *et al.* 2022, 2023), established a baseline for multicomponent imaging (Markovic *et al.* 2023), presented a preliminary characterization of ambient noise in the area (Kaslilar *et al.* 2022), and assessed a surface-wave dispersion of the passive and active source data sets (Wilczynski *et al.* 2023).

This paper focuses on the ambient noise data recorded with the 2-D seismic active source experiment. The profile begins in the northwest, near the mineralization lineament, and runs 2400 m southeast, parallel to the dip direction of the mineralization. According to the bedrock geology map (Fig. 1b), the profile extends over four lithologies: metagranitoid intrusion, rhyodacitic, and rhyolitic metavolcanic rocks, and again a metagranitoid intrusion. It cuts through a mineral prospect in the middle and a deformation zone at the southern end, followed by a smooth elevation change of 20 m (Fig. 1a).

The bedrock is covered with a thin layer of sediments (no more than 20 m), mostly till and glacial silt–sand deposits – with an occasional presence of peat and flood deposits (Fig. 1d). Several small water streams are present and run east or northeast. In the south, the profile reaches a rather idle national road no. 50 and a railway used by freight and passenger trains. The localities of Blötberget and Klenshyttan are situated at the northern and southern ends of the profile, respectively, and several properties are located near the profile (backfill in Fig. 1d). These features are potential sources of seismic noise.

We attempt to image the geological contacts and other subsurface features important for mineral prospecting. The ambient noise investigation is supplemented with (i) active source seismic data, (ii) geodata courtesy of Geological Survey of Sweden (SGU 1988, 2014, 2018a, b) presented on maps in Figs 1(b)–(d), (iii) rock properties information from geophysical well-logging (Maries *et al.* 2017), (iv) cored borehole information, courtesy of Nordic Iron Ore, (v) previous seismic reflection studies delineating the mineralization (Pertuz *et al.* 2021), (vi) shallow subsurface shear-wave velocity estimated by Papadopoulou *et al.* (2019), and (vii) airborne residual magnetic field measurements courtesy of SGU (Fig. 1c).

3 DATA AND METHOD

The following subsections outline our investigation workflow. We started by analysing the raw active source data to understand the velocity distribution in the medium and identify disruptive events. We then processed the passive data and performed surface-wave analysis to produce a shear-wave velocity section. Finally, we validated our findings with active source data and provided a comprehensive result by merging the passive and active data sets.

3.1 Active source data – initial analysis

The active data in this study were collected using 492 vertical-component micro-electromechanical system (MEMS) accelerometers and a 77 kN peak force vibrator as a source with a linear sweep from 2 to 200 Hz (Gyger *et al.* 2022). The receivers were spaced every 5 and covered over 2400 m of a nearly linear seismic array (Fig. 1a). Taking advantage of their broadband nature, the sensors were recording frequencies from 1.25 to 200 Hz. The raw seismic traces were cross-correlated with a theoretical sweep, corrected for statics, and balanced for a better display (Gyger *et al.* 2023). An example shot gather from the centre of the spread is presented in Fig. 2(a). The signal energy is relatively low in a frequency band of up to 20 Hz. It reaches its peak above 30 Hz and preserves high energy until around 150 Hz.

We assume that, due to shallow compressional fracturing or weathering, the bedrock can be characterized by a velocity gradient. To test this hypothesis, we conducted a simple arrival time analysis. We used the picked first break traveltimes corrected with the static solution to estimate the average velocity gradient in the medium. To find the velocity gradient, we used a diving wave equation $t_i = \frac{2}{k} * \frac{\sinh^{-1}(kx_i)}{2v_0}$ where t_i and x_i are the arrival time and the offset at an individual trace (respectively), k is the P-wave velocity gradient per meter of depth, and v_0 is the initial velocity at the surface.

The data fitting results were: initial velocity v_0 of 5170 m s^{-1} and the vertical gradient k of 2.75 m s^{-1} per meter of depth. The R-squared goodness of fit was more than 99 per cent. The Vp/Vs ratio in the igneous rocks in the area, based on geophysical well-logging, ranges from 1.4 to 1.8 (Maries *et al.* 2017), and we assumed the Vp/Vs ratio equal to 1.8 for this experiment. Adding the sediment layer information from the nearby cored borehole (Fig. 1a), and the shear-wave velocity in the bedrock from a surface-wave study of Papadopoulou *et al.* (2019), we constructed a 1-D velocity model (Table 1).

We used a finite-difference elastic modelling software (Thorbecke & Draganov 2011) to generate a synthetic shot gather (Fig. 2b) given the velocity model provided in Table 1. By comparing the traces from both data sets, we verified the initial general assumption of a velocity gradient in the shallow bedrock, which served as a baseline for the following steps. The similarity between the data sets is discussed later.

Moreover, in the raw shot gathers, we observed signal scattering signatures originating from traces 187, 290, 340, 380 and 440 (Figs 3a–c; CMPs 1400, 1580, 1700, 1770 and 1900). These features suggest subsurface features and are referred to further in this paper.

3.2 Passive data

The passive data recording took place along with the active source campaign, using the same receivers installed in the field in the

Downloaded from https://academic.oup.com/gji/article/240/1/571/7875257 by Witwatersrand Health Sciences Library user on 08 August 2025

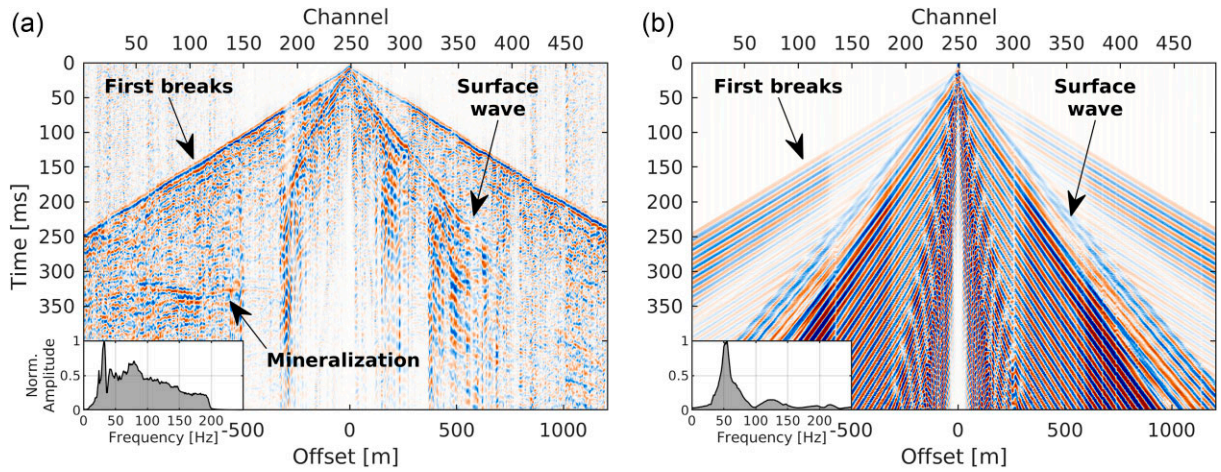


Figure 2. Shot gathers from the centre of the spread (shot point 250) and corresponding normalized amplitude spectra. (a) Active source shot gather with static corrections applied. (b) Synthetic shot gather generated with the velocity model from Table 1.

Table 1. 1-D velocity model estimated from first break traveltimes and *a priori* information from Maries *et al.* (2017) and Papadopoulou *et al.* (2019). Depth represents depth to the top of the layer.

Layer	Depth (m)	V_p (m s^{-1})	V_s (m s^{-1})	ρ (kg m^{-3})
Glacial sediments		1200	500	2200
Weathered bedrock	4.25	5170	2600	2650
Gradient [1/m]		+2.77	+1.80	+0.3
Bedrock	300	6000	3140	2750

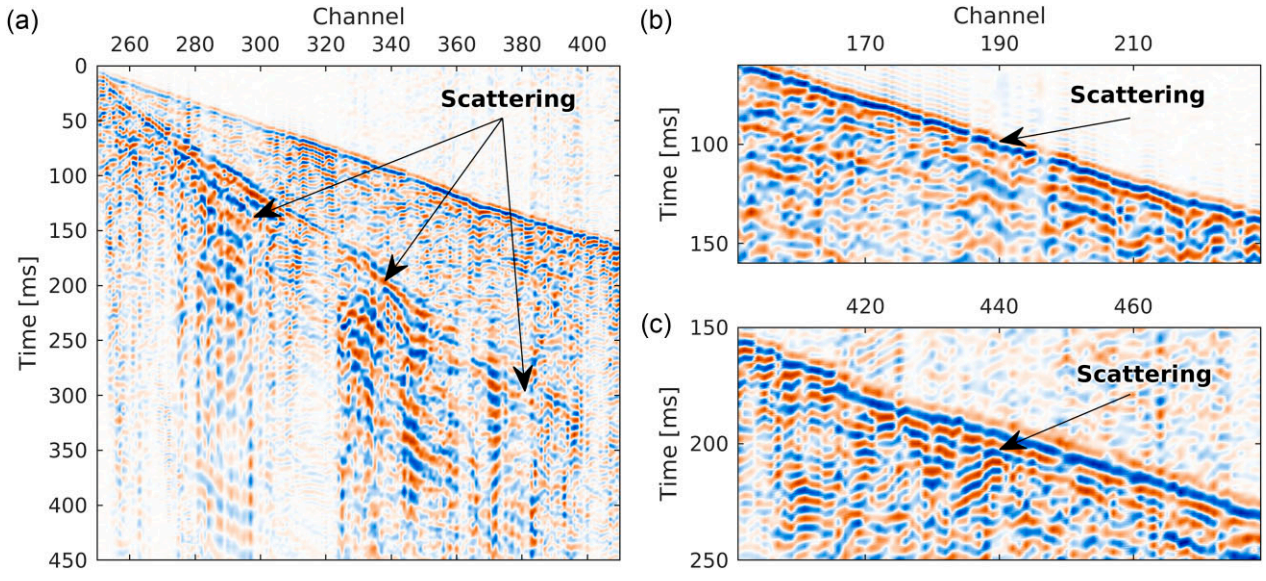


Figure 3. Close-ups of the scattering features observed in active source data. (a) Shot gather 250, channels 290, 340, 380 (CMPs 1580, 1700 and 1770). (b) Shot gather 100, channel 187 (CMP 1400). (c) Shot gather 250, channel 440 (CMP 1900).

Downloaded from https://academic.oup.com/gji/article/240/1/571/7875257 by Witwatersrand Health Sciences Library user on 08 August 2025

nearly linear array. We collected the data for four consecutive days and nights (2022 June 16–20), but used only the nighttime data (22:00 to 06:00), totalling 32 hr of recording.

3.2.1 Processing

We followed the processing scheme suggested by Yao *et al.* (2006) and used 32 1-hr long records, downsampled to 8 ms sampling frequency (62.5 Hz Nyquist frequency). The pre-processing steps included spectral whitening of the signals, splitting them in frequency bands at cut-off frequencies between 2 and 40 Hz, 1-bit normalization and stacking to broadband 1-bit normalized traces. For each station pair, the pre-processed hourly records were cross-correlated and stacked. The resulting cross-correlation functions (CCF) are approximations of Green's functions (Yao *et al.* 2006; Bensen *et al.* 2007).

We sorted the cross-correlograms to virtual source points (Fig. 4a), presenting results of cross-correlation of all receivers with a single receiver acting as a virtual source (Bakulin & Calvert 2006; Snieder *et al.* 2006). We observe strong Rayleigh-wave arrivals, with an apparent velocity of 2400 m s^{-1}, and airwave arrivals (Fig. 4b). A low symmetricity between the causal and acausal parts of the CCF suggests a noise directionality. To evaluate the noise sources distribution, we performed MUSIC beamforming as presented by van den Ende & Ampuero (2021) and Zhao *et al.* (2023), and analysed the direction of the source in a frequency band of 12–14 Hz in which we expect the observable wavelengths. The main energy sources are located southeast of the array (Fig. 4a), most likely at the national road and the railway (Fig. 1a). Such noise distribution allows for an unbiased phase velocity estimation (Foti *et al.* 2007; Park *et al.* 2007; Pang *et al.* 2023).

We resorted the data to keep only the clear surface-wave arrivals, i.e. the causal part of the negative-offset traces (quarter 3 in Fig. 4a) and the acausal part of the positive-offset traces (quarter 1 in Fig. 4a). Thus, we removed the other two quarters (causal part positive offsets and acausal part negative offsets, quarters 2 and 4) and flipped the acausal part (quarter 1). In this way, we constructed a virtual shot gather (Fig. 4b).

With this processing and data handling sequence, we obtained 492 virtual shot gathers with clear Rayleigh-wave arrivals. Most energy is concentrated in the 2.5 to 20 Hz frequency band (Figs 4a and b), showing the expected advantage over the active source data in the low-frequency band. A few energy peaks at higher frequencies can be related to anthropogenic sources (e.g. properties at backfill in Fig. 1d). The Rayleigh-wave signature is clear at most traces, with a few zones of signal disturbance, e.g., channels 75, 150, 180, 360 and 430. Their position collocates with the water streams or brooks flowing nearby, and the last two with private property facilities (backfill layer in Fig. 1d). The disturbances are local, contaminating only a few neighbouring traces. We expect these traces to have a low impact on the surface-wave analysis due to a high level of data redundancy (Park *et al.* 1999). We observe only one artefact significantly disturbing the Rayleigh-wave arrival (black arrows in Figs 5a and b). Its source is colocated with a scatterer observed in active source data (Fig. 3b).

For better control of the point of investigation, we resorted the data from virtual shot gathers to common mid-point (CMP) gathers. The CMP gathers use source–receiver combinations from different shot gathers, lowering the possible influence of noisy virtual shot gathers. Due to the reciprocity of cross-correlation, and because we used the causal and the flipped acausal parts of the CCFs, the CMP gathers are perfectly symmetric around the midpoint. Thus, we keep only the positive offsets for further investigation.

3.2.2 Surface wave analysis

We performed MASW analysis using the frequency-wavenumber (FK) method implemented in the Geopsy tool (Wathelet *et al.* 2020). The relative arrival times at each station are used to calculate the phase shifts. The array output (semblance) is obtained by summing the shifted signals in the frequency domain and normalizing them by spectral power (Wathelet 2005). Our workflow for each point, including data muting, dispersion curve extraction, and inversion, is presented in Fig. 6 and subfigures therein.

The array capability of unaliased extraction of surface-wave modes depends on the array parameters, such as number of stations, source–receiver offset, and array length. According to the Nyquist theorem, the maximum wavenumber k_{max} that can be sampled is $\frac{\pi}{\Delta x}$, where Δx is the interstation distance. This relation determines the minimum recoverable wavelength $\lambda_{min} = 2\Delta x$. In theory, the array geometry should not constrain the minimum recoverable wavenumber (or maximum wavelength) (Park & Miller 2008). However, the array resolution depends on the site's global behaviour (Socco & Strobbia 2004) and the introduced measurement uncertainties (Park & Miller 2008). Practitioners show that wavelengths up to twice the length of the array can be recovered with minimal error in phase velocity estimation (Park *et al.* 1999), with a general rule of thumb suggesting using an array length equal to the expected wavelength (Foti *et al.* 2018). Lengthening the array increases the wavenumber resolution and, consequently, allows for observing longer wavelength and reducing the uncertainty in the low-frequency band (Foti *et al.* 2018). However, MASW assumes a layered earth model of the elastic properties and, when lateral variations are suspected, requires arrays as short as possible to maximize the validity of this assumption (Park *et al.* 1999). Thus, the decision on the array length is a trade-off between a wavenumber resolution of the array (and thus longer observable wavelengths and depths of investigation) and the lateral reliability of the solution.

Due to the short receiver spacing (5 m), the minimum recoverable wavelength λ_{min} is 10 m, which is shorter than the shortest expected wavelength propagating in the medium (20 m for 500 m s^{-1} velocity and 25 Hz frequency). Thus, we do not need to include the maximum wavenumber limit in further considerations. As for the minimum wavenumber limit k_{min}, we aimed for the array lengths of 300 m to be able to reach the highest observable wavelengths λ_{max} of 300 to 600 m, which we expect at 5 Hz frequency (and 3000 m s^{-1} Rayleigh-wave velocity). Using lower frequencies (down to 2.5 Hz) and recovering wavelengths up to 1200 m would require roughly half of the seismic profile and constrain the obtained model's lateral resolution.

In active source surface-wave analysis, it is common practice to account for the near-source effects (Park *et al.* 1999; Socco & Strobbia 2004), caused by the waveform behaviour in short offsets. Ryden & Mooney (2009) suggested using a minimum offset longer than one wavelength. We expect the railroad and the country road at the end of the profile (Fig. 1a) to be the main energy sources, but we do not observe near-source effects in the virtual shot gathers. Nevertheless, we aim for a source-array offset of 50 m to avoid the undesired effects of muting parts of the cross-correlograms. Hence, we aimed for 50–350 m array geometry, with 5 m receiver spacing Δx.

Downloaded from https://academic.oup.com/gji/article/240/1/571/7875257 by Witwatersrand Health Sciences Library user on 08 August 2025

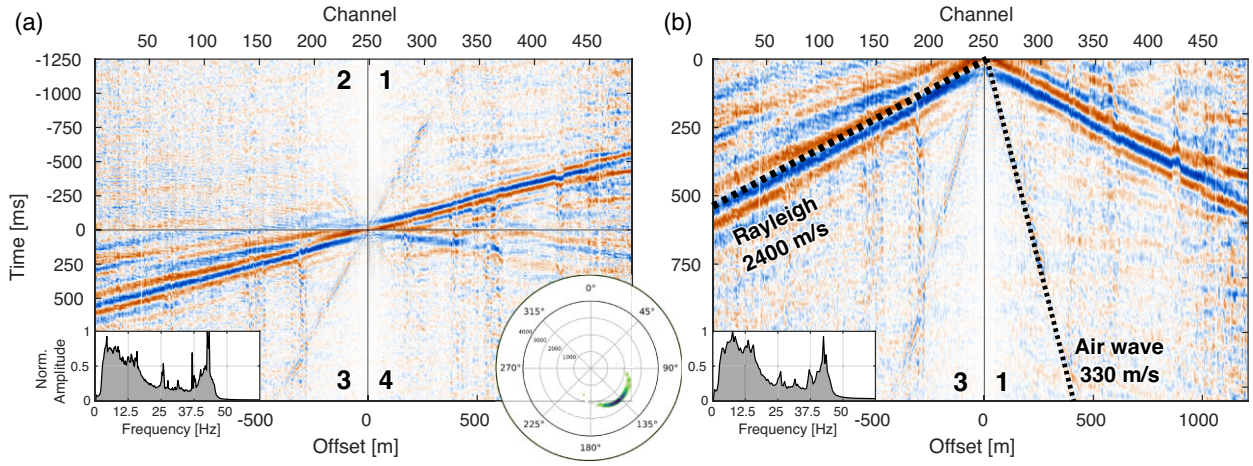


Figure 4. Cross-correlogram for a virtual shot point 251 (centre of the spread) and corresponding normalized amplitude spectra. Numbers mark quarters discussed in the main text. A radial plot in the centre presents a distribution of the back-azimuth of the most energetic sources (upper 60 per cent) in a frequency band of 12–14 Hz. (a) Cross-correlogram with both causal and acausal parts of the correlation. (b) A virtual shot gather constructed of causal and acausal parts of the cross-correlogram. The Rayleigh wave and airwave arrivals are marked with dotted lines.

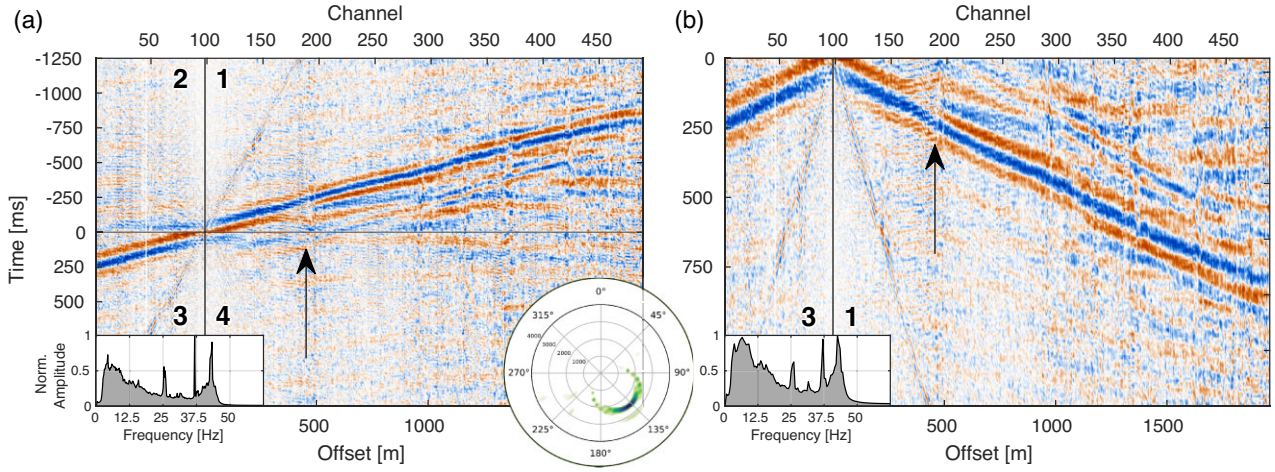


Figure 5. Cross-correlogram for a virtual source point 100, presenting a disruptive event around channel 200 (black arrow), and corresponding normalized amplitude spectra. Numbers mark quarters discussed in the main text. A radial plot in the centre presents a distribution of the back-azimuth of the most energetic sources (upper 60 per cent) in a frequency band of 12–14 Hz. (a) Cross-correlogram with both causal and acausal parts of the correlation. (b) A virtual shot gather constructed of causal and acausal parts of the cross-correlogram.

We applied the tapered top- and bottom-mutes to the ANSI-retrieved data to focus our analysis on the Rayleigh-wave arrivals (Fig. 6a) and performed MASW for every fifth CMP (every 12.5 m along the profile). The assumed array geometry was not always optimal, and we modified the offset ranges when necessary to achieve the best results. However, regardless of the source-array offset, the obtained semblance corresponded to fixed coordinates due to the data being sorted into CMP gathers. Modifying the offset ranges was particularly useful when processing the CMP gathers contaminated with the artefact presented in Figs 5(a) and (b).

We computed synthetic Rayleigh dispersion curves from the previously established 1D velocity model (Table 1). We displayed it with the phase velocity–frequency spectra (Fig. 6b) to use it as a guide in dispersion curve extraction. Then, we carefully extracted surface-wave dispersion curves following the maximum semblance values and taking into consideration the array resolution limits $k_{\min}$ and $k_{\min}/2$. In the synthetic curve, the higher mode does not appear at frequencies lower than 20 Hz, hence we assume that the extracted apparent curve represented the fundamental mode.

The extracted DCs are presented in Fig. 7, with wavelength pseudosection and used array lengths and source-array offsets in Fig. 8. The velocities varying with frequencies prove the initially assumed dispersive nature of the medium. We did not recover any information for velocities lower than 2000 m s^{-1}, and most of the curves were confined within the 6 to 16 Hz range.

We have observed that the dispersion curves showed a variation in velocity along the profile, with wavelengths shortening towards the end of the profile. The average value of the extracted dispersion curves is consistent with the synthetic dispersion curve. Additionally, the curves from the beginning of the profile (CMPs 1100 to 1500) exhibit high-velocity and long wavelengths. Distinct low-velocity anomalies around CMP 1400, 1580 and 1770 correspond to the locations of previously observed scatterers.

Downloaded from https://academic.oup.com/gji/article/240/1/571/7875257 by Witwatersrand Health Sciences Library user on 08 August 2025

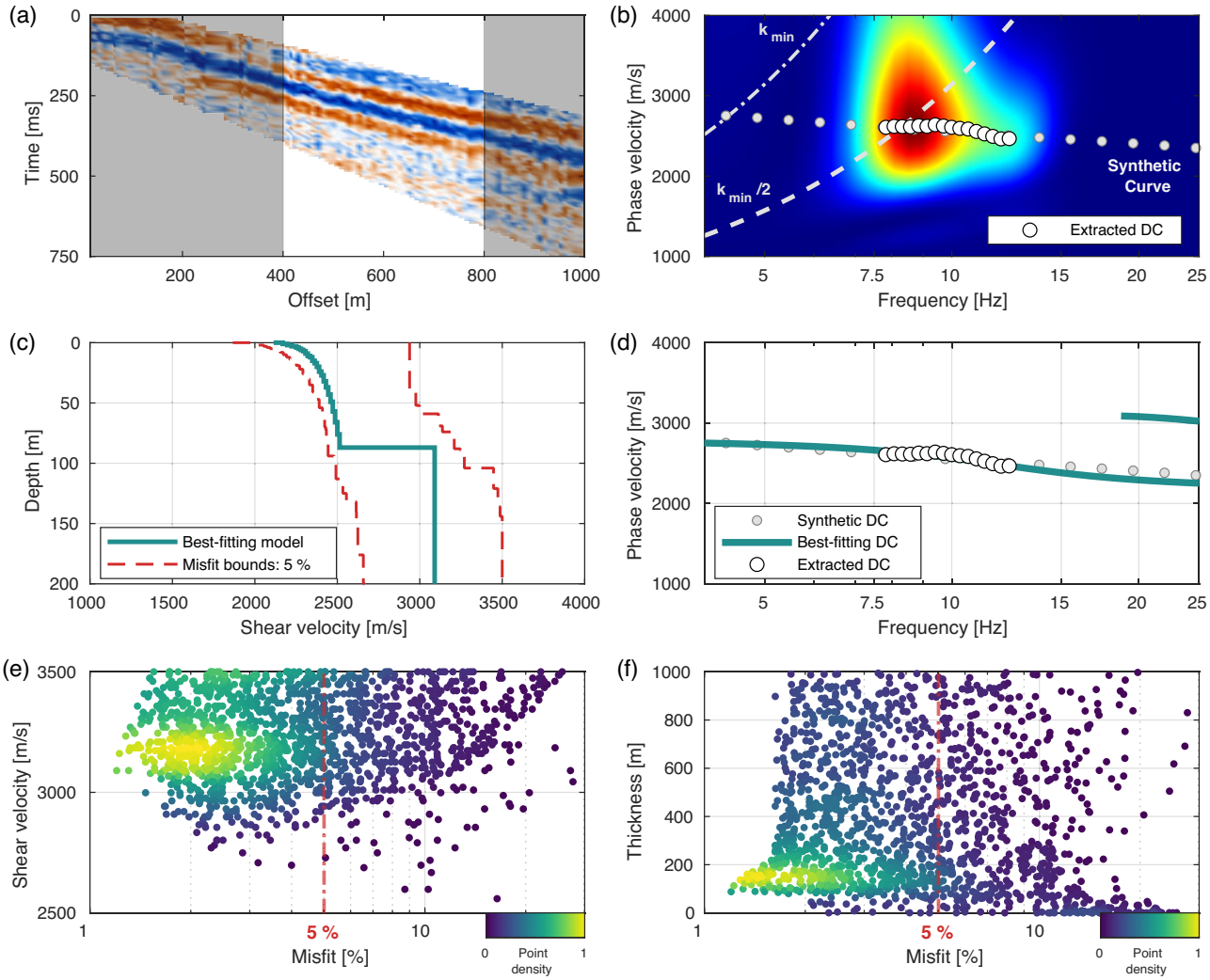


Figure 6. Presentation of the components of the surface-wave analysis (passive data) for virtual CMP 1340. (a) Noise-retrieved CMP gather with top and bottom mutes around the surface-wave arrival. Grey and white polygons present the used array length and source-array offset. (b) Frequency-phase velocity matrix (semblance) with wavenumber resolution limits $k_{\min}$ and $k_{\min}/2$ and the synthetic fundamental mode dispersion curve from a velocity model in Table 1. The *X*-axis in logarithmic scale. (c) 1-D shear-wave velocity model from the dispersion curve inversion. The best-fitting model has the lowest obtained misfit. (d) Comparison of the extracted DC with dispersion curves corresponding (fundamental and first higher mode) to the best-fitting model and a synthetic curve from the model in Table 1. (e) Parameter space for the shear-wave velocity of the halfspace (bedrock). (f) Parameter space for the thickness of the first layer (weathered bedrock).

3.2.3 Inversion

The maximum depth of investigation for the MASW method is assumed to range from $\lambda/3$ to $\lambda/2$ (Park *et al.* 1999; Socco & Strobbia 2004; Foti *et al.* 2018). With the shortest wavelength λ around 150 m, we could not resolve for the shallowest 50–75 m of the subsurface. Therefore, with the maximum soil thickness in the area lower than 20 m (SGU 2014), we did not expect to resolve for the soil layers. Additionally, we observe a velocity gradient in the active source data. Based on these observations, we parametrized inversion for two layers only: weathered bedrock and bedrock, with the first layer velocities following a power-law gradient. The *S*- and *P*-wave velocities were constrained from 1500 to 3500 m s^{-1} and 2500 to 6500 m s^{-1}, respectively. Following the findings of Maries *et al.* (2017) and recommendations of Casto *et al.* (2009), we set the Poisson's ratio values between 0.1 and 0.35 and used a fixed density of 2750 kg m^{-3}. The thickness of the first layer was constrained between 0 and 1000 m.

We used the extracted dispersion curves as input for inversion for 1-D velocity models at each analysed CMP. We used the neighborhood alhorithm (Wathelet 2008), implemented in Geopsy tool (Wathelet *et al.* 2020). It is a direct search method, with generated models being guided by the results obtained so far on the previous samples. We parametrized 1000 iterations, starting from 500 initial models and preserving the 50 best cells of the lowest misfit in each iteration. The generated models are evaluated using a misfit between the input curve and a forward response of the model. The lowest-misfit model is outputted as the best-fitting (Figs 6c and d).

First, we assessed the inversion by comparing the extracted curve with the best-fitting model dispersion curve (Fig. 6d), and then by examining the parameter space plots showing values obtained by all models for a given parameter. Figs 6(e) and (f) present two

Downloaded from https://academic.oup.com/gji/article/240/1/571/7875257 by Witwatersrand Health Sciences Library user on 08 August 2025

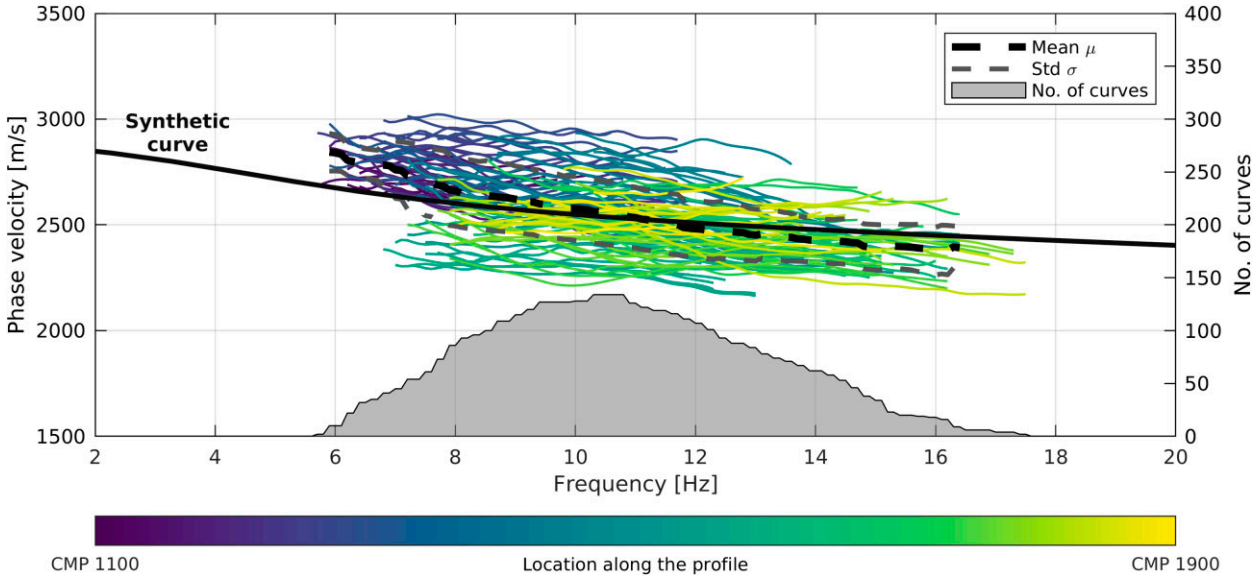


Figure 7. Ambient noise dispersion curves extracted along the profile with the synthetic fundamental mode dispersion curve obtained with a velocity model in Table 1 and calculated mean and standard deviation. The right *Y*-axis corresponds to the number of dispersion curves with a particular frequency (grey area). The colour scale corresponds to the position along the line.

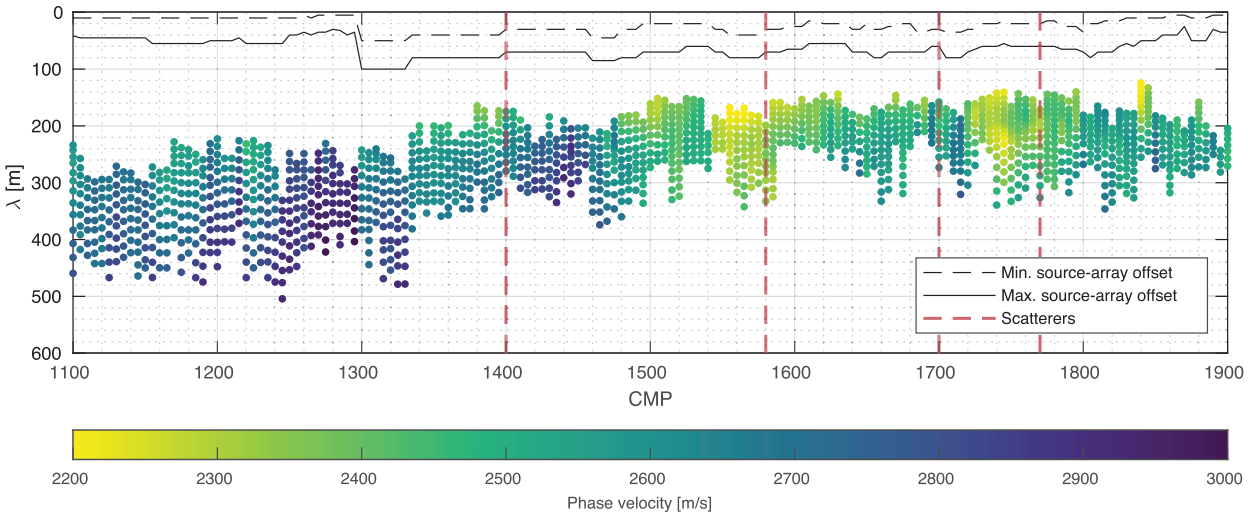


Figure 8. A pseudosection of dispersion curves extracted from ambient noise along the profile with phase velocity colour scaling. The vertical dashed lines present the position of the scatterers observed in the active data (Fig. 3). The black lines (dashed and solid) present the source-array offset and array length, scaled by 1/10 factor for a better display.

parameter space plots: the half-space (bedrock) shear-wave velocity and the thickness of the first layer (weathered bedrock), representing the depth to the half-space. The best-fitting model is at the tip of the fan-like distribution of models.

After applying the procedure to every fifth CMP, we interpolated the results to a 1 m cell size and then smoothed using a 2-D Gaussian filter with a width of 301 m and a depth of 15 m. This process allowed us to construct a 2-D shear-wave velocity model based on the 1-D velocity models for CMPs along the line, presented in Fig. 9. However, due to the long wavelengths of the used dispersion curves (minimum 150 to 250 m), the velocity profile resolution in the upper ca. 75 m is limited (marked by the white-shaded area in Fig. 9).

3.3 Active source data – validating the results

In order to confirm our findings and to provide resolution in the shallow part of the profile, we performed the active source surface-wave analysis preserving the same investigation workflow. The active source data, characterized by the same geometry as the passive data, was resorted to CMP gathers. Apart from trace balancing, static corrections, and muting, no further processing was applied. We performed the surface-wave analysis using a similar workflow as for the passive data. A comprehensive example of active source surface-wave analysis, similar to Fig. 6 for passive data, is shown in Fig. 10 and its subfigures.

Downloaded from https://academic.oup.com/gji/article/240/1/571/7875257 by Witwatersrand Health Sciences Library user on 08 August 2025

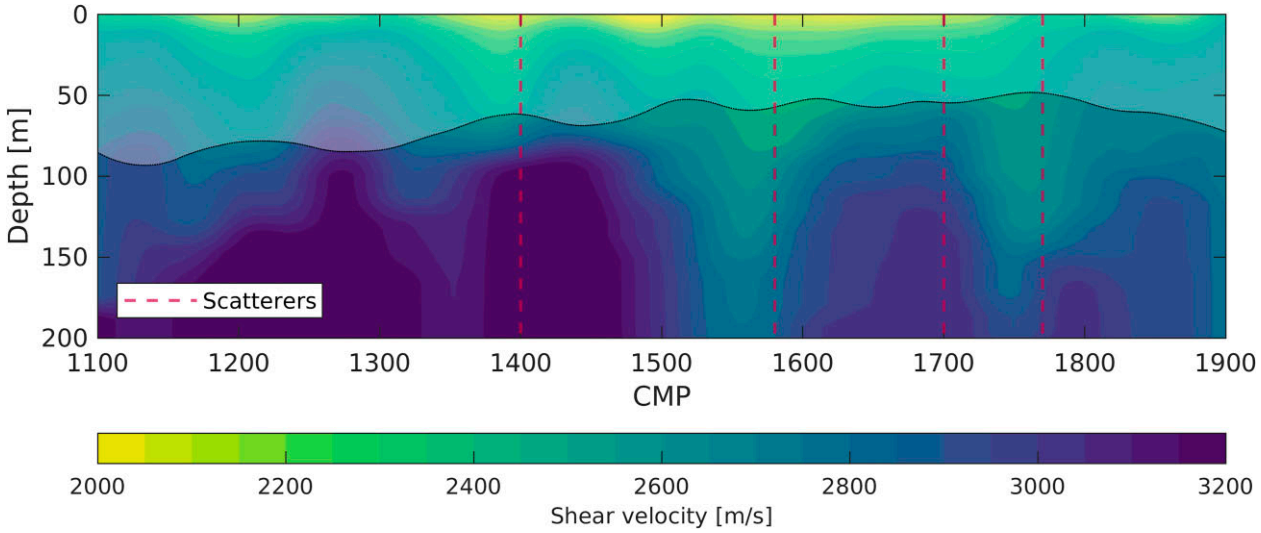


Figure 9. A smoothed passive data 2-D shear-wave velocity section constructed from 1-D models for every fifth CMP. The vertical dashed lines present the position of the scatterers observed in the active data (Fig. 3). The white-shaded area presents the minimum resolution limit according to the $\lambda/3$ criterion. Colour scale limits were clipped for a better comparison with other data sets.

For every fifth CMP, we conducted the surface-wave analysis using the signals muted around the surface-wave arrival (Fig. 10a). We aimed at the array length similar to the passive data workflow (300 m) to calculate the phase velocity and frequency spectrum (Fig. 6b). However, we had to change the source-array offset to 100 m to take into account the near-source effects, sometimes extending it to longer distances. Compared to the passive data, the extracted dispersion curves ranged over lower velocities due to a higher frequency content. Thus, they provided much shorter wavelengths and a higher resolution in the shallow subsurface to ca. 75 m. The dispersion curves are presented in Fig. 11, and the wavelength pseudosection with array lengths in Fig. 12.

We accounted for the lower phase velocities by parametrizing a low-velocity layer in the inversion scheme. According to the soil depth maps of the Geological Survey of Sweden (SGU 2014), the sediment layer thickness does not exceed 20 m and consists mostly of glacial tills (Fig. 1d). Thus, we constrained the layer in a range of 0–20 m of thickness, a fixed density of 2500 kg m^{-3}, 0.1 to 0.5 Poisson's ratio, 1000–2000 m s^{-1} shear-wave velocity, and 1000–2300 m s^{-1} compressional-wave velocity. Another layer, following the power-law velocity gradient, and a half-space were parametrized as in the passive data inversion.

Many models satisfied the 5 per cent misfit criterion (Figs 10e and f), with the lowest misfit being at the tip of the parameter space fan. Same as for the passive data, we constructed a smoothed 2-D shear-wave velocity profile (Fig. 13). Assuming a maximum recoverable depth following the $\lambda/2$ relation, we did not expect the results to be credible at depths greater than ca. 75 m (white shaded area in Fig. 13).

3.4 Passive and active data – merged results

The dispersion curves and recovered wavelengths in the active data set complimented the short-wavelength gap in the passive data set. We combined both DCs corresponding to a single CMP and obtained a single curve with information from both the passive data (low frequencies and long wavelengths) and the active source data (high frequencies and short wavelengths).

The combined curves are presented in Fig. 14. The frequency range spanned from 6 to 50 Hz and corresponded to velocities from 3000 to 1500 m s^{-1}. The wide range of wavelengths and velocities provided a broad wavelength distribution (Fig. 15). The number of curves around 15 Hz is lower, indicating that not all CMPs had overlapping curves.

We inverted the merged curves using the same inversion parametrization as for the active data set, with a shallow layer of sediments. We did not smooth the curves nor interpolate them in the gaps but allowed the inversion to find the best-fit. For each point, we managed to satisfy the 5 per cent misfit criterion and proceeded with the best-fitting model. Then, we constructed a 2-D smoothed shear-wave velocity profile, presented in Fig. 16. The broad range of recovered wavelengths provides a resolution to a depth of ca. 200 m.

In the shear-wave velocity profile shown in Fig. 16, we observed several features: a low-velocity layer reaching a depth of 20 m, high-velocity zones spanning from CMP 1100 to 1500, a moderately high-velocity zone between CMP 1600 and 1900, a low-velocity zone from CMP 1720 to 1780, with distinct scattering features, and a low-velocity zone in the centre of the profile (CMP 1500 to 1600) with a marked sharp lateral boundary around the position of an observed scatterer. Importantly, these features (excluding the shallow low-velocity layer) are also present in the passive data section (Fig. 9).

4 RESULTS

Our work focused primarily on obtaining the shear-wave velocity distribution from ambient seismic noise in a typical reflection seismic setting (2400 m long 2-D line). We used a conventional processing scheme and obtained results down to a moderate depth (ca. 200 m). We validated our results with active source data and complemented them with information about the shallow depths, where the passive seismic method has limited resolution.

Downloaded from https://academic.oup.com/gji/article/240/1/571/7875257 by Witwatersrand Health Sciences Library user on 08 August 2025

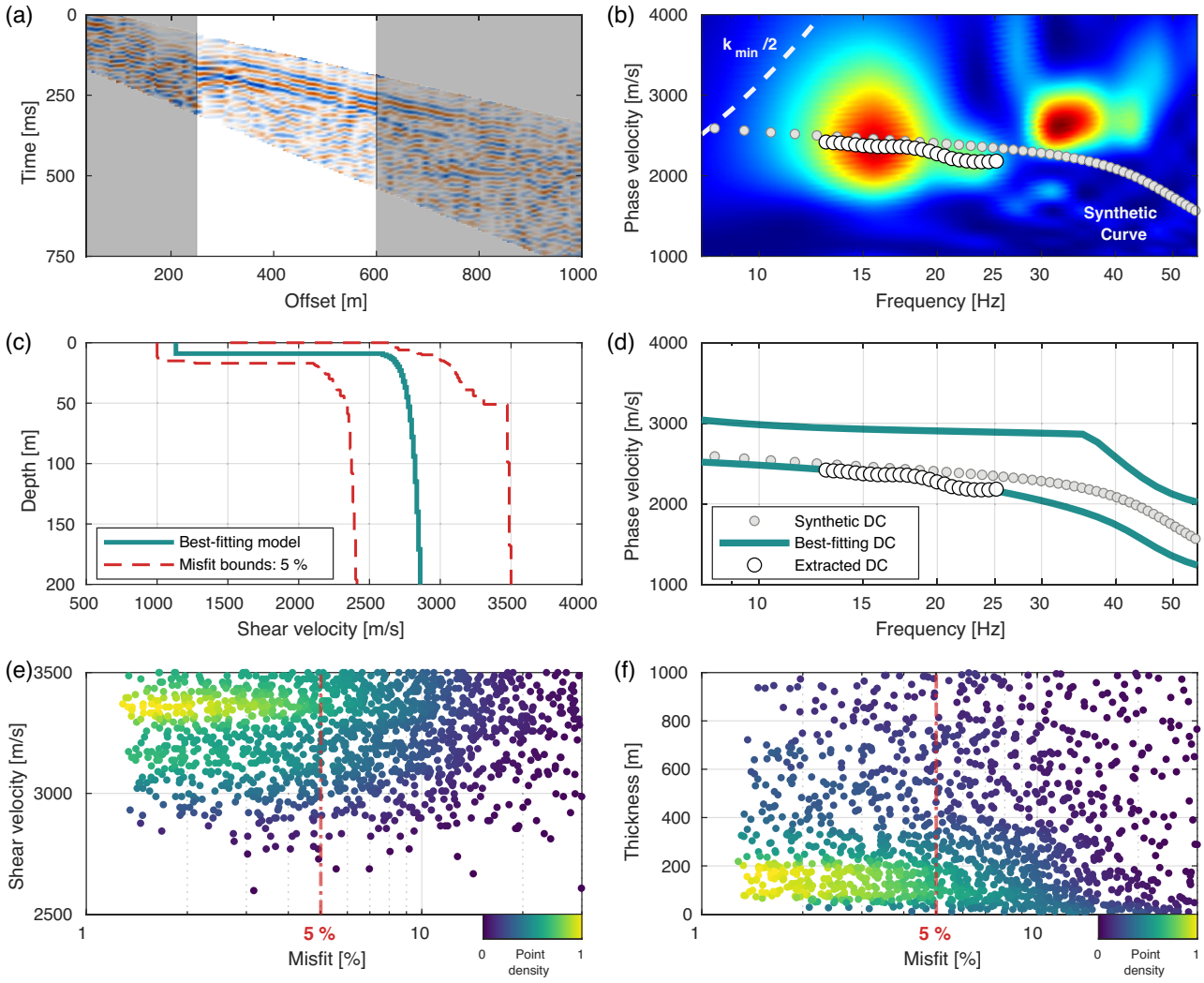


Figure 10. Presentation of the components of the surface-wave analysis (active source data) for virtual CMP 1340. (a) Noise-retrieved CMP gather with top and bottom mutes around the surface-wave arrival. Grey and white polygons present the used array length and source-array offset. (b) Frequency-phase velocity matrix (semblance) with wavenumber resolution limits $k_{\min}$ and $k_{\min}/2$ and the synthetic fundamental mode dispersion curve from a velocity model in Table 1. The *X*-axis in logarithmic scale. Note a longer frequency axis than in Fig. 6(b). (c) 1-D shear-wave velocity model from the dispersion curve inversion. The best-fitting model has the lowest obtained misfit. (d) Comparison of the extracted DC with dispersion curves corresponding (fundamental and first higher mode) to the best-fitting model and a synthetic curve from the model in Table 1. (e) Parameter space for the shear-wave velocity of the half-space (bedrock). (f) Parameter space for the thickness of the second layer (weathered bedrock).

Using the ambient noise, we reached depths of several hundred meters thanks to the low-frequency content and high-medium velocities. The obtained shear-wave velocities of the bedrock spanned from 2100 to 3300 m s^{-1}. However, due to the long wavelengths, the received models were not credible at depths shallower than approximately 75 m.

We improved the resolution of the shallower part using the active source data. We provided a shear-wave velocity profile for the active data for the upper approximately 75 m, imaging a shallow soil layer to a depth of 20 m. Additionally, we combined the two data sets, which allowed us to resolve both the shallow layers and the subsurface down to 200 m depth, thanks to broadband dispersion curves obtained from the merged data sets. The depths of investigations and other characteristics are presented in Table 2.

The passive data section in Fig. 9 and the merged data section in Fig. 16 show high similarity at greater depths (more than ca. 75 m), which were penetrated by the low-frequency ambient noise surface waves. It exhibits similar velocity features, with significant low-velocity zones. The primary distinction is a shallow low-velocity layer to a depth of 20 m, which is beyond the resolution of the passive data. Moreover, the mentioned deep features are less apparent in the active source profile in Fig. 13 due to the lower resolution at depths greater than ca. 75 m.

5 DISCUSSION

In this section, we discuss the quality of the results taking into account possible acquisition and processing improvements, and provide a geological interpretation of the obtained

Downloaded from https://academic.oup.com/gji/article/240/1/571/7875257 by Witwatersrand Health Sciences Library user on 08 August 2025

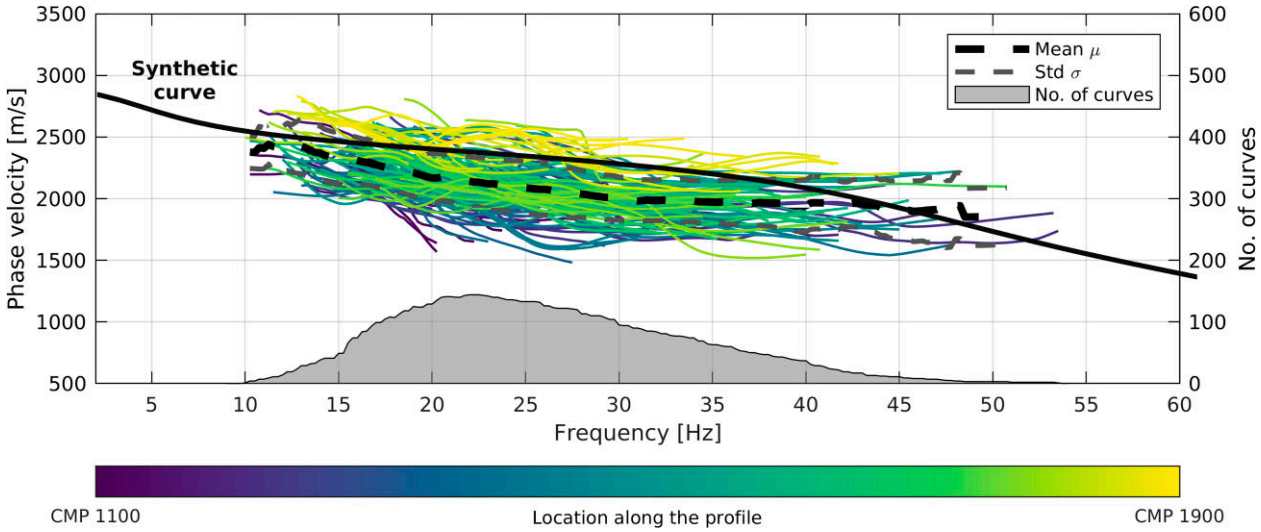


Figure 11. Active source dispersion curves extracted along the profile with the synthetic fundamental mode dispersion curve obtained with a velocity model in Table 1 and calculated mean and standard deviation. The right *y*-axis corresponds to the number of dispersion curves with a particular frequency (grey polygon). The colour scale corresponds to the position along the line. Note a longer frequency axis than in Fig. 7.

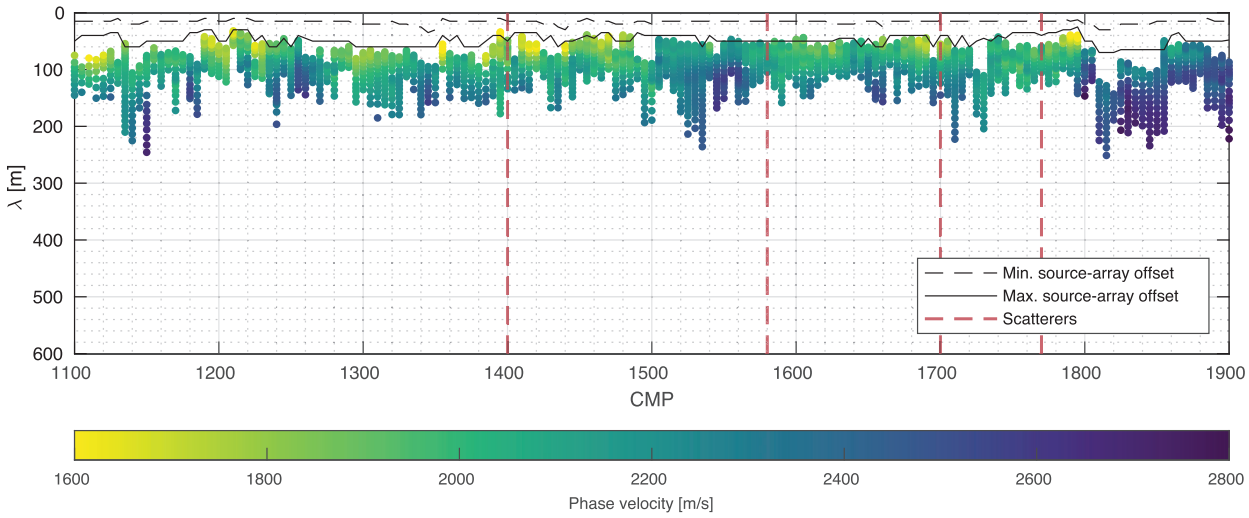


Figure 12. A pseudosection of active source dispersion curves extracted along the profile with phase velocity colour scaling. The vertical dashed lines present the position of the scatterers observed in the active data (Fig. 3). The black lines (dashed and solid) present the source-array offset and array length, scaled by 1/10 factor for a better display.

results, supporting our reasoning with the previously available data. We also discuss the versatility of the method and its potential applications in hardrock mineral exploration and other environments.

5.1 Data, processing and results quality

As a baseline for our investigation, we observed a velocity gradient in the first break traveltimes in the active source data. We used it with the borehole information to model a synthetic shot gather. Then, we retrieved the seismic arrivals from the ambient noise data and sorted the data into virtual shot-gathers. We present all three shot gathers (synthetic, active source and passive) in Figs 17(a)–(c). We filtered the data to the passive data surface-wave frequency band (6–16 Hz) and calculated the semblance to evaluate the similarity between the data sets. We used a simplified semblance equation $S^i_{XY} = 1/2 + \frac{R^i_{XY}(0)}{R^i_{XX}(0)+R^i_{YY}(0)}$, where semblance S for a trace i of X, Y data sets is calculated as a ratio of correlations R at zero lag.

The obtained semblance for channel 375 for active and synthetic traces S^{375}_{AS} was 0.95, and for active and passive S^{375}_{AP} reached 0.86, proving high similarity of the waveforms in this frequency band (6–16 Hz) and validity of the used velocity model (Table 1). We compare the traces and present the semblance in Fig. 17(d). The same apparent velocity characterizes the noise-retrieved surface waves as in the active source data, and the inline noise distribution ensured unbiased phase-velocity measurements. Moreover, the virtual shot gather demonstrates an advantage in the lower frequency band, with a high-energy concentration already at 2 Hz, compared to 20 Hz in the active source experiment.

In the ambient noise surface-wave analysis, we obtained several hundred meters of investigation depth thanks to particularly long wavelengths (up to 500 m), which are a result of the high-seismic

Downloaded from https://academic.oup.com/gji/article/240/1/571/7875257 by Witwatersrand Health Sciences Library user on 08 August 2025

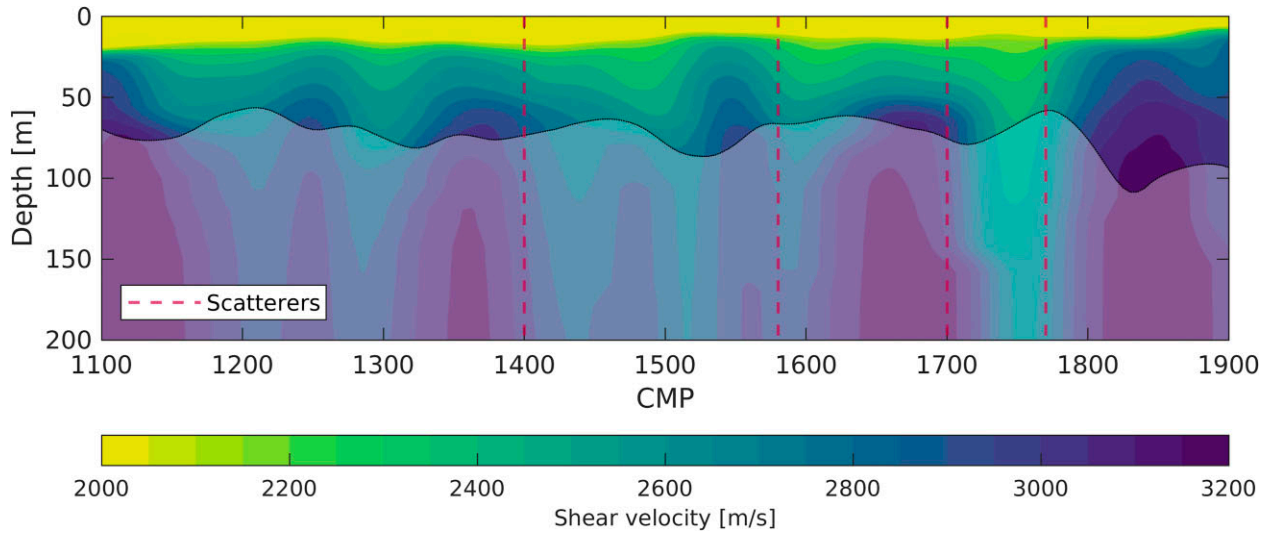


Figure 13. A smoothed active-data 2-D shear-wave velocity section constructed from 1-D models for every fifth CMP. The vertical dashed lines present the position of the scatterers observed in the active data (Fig. 3). The white-shaded area presents the maximum resolution limit according to the $\lambda/2$ criterion. Colour scale limits were clipped for a better comparison with other data sets.

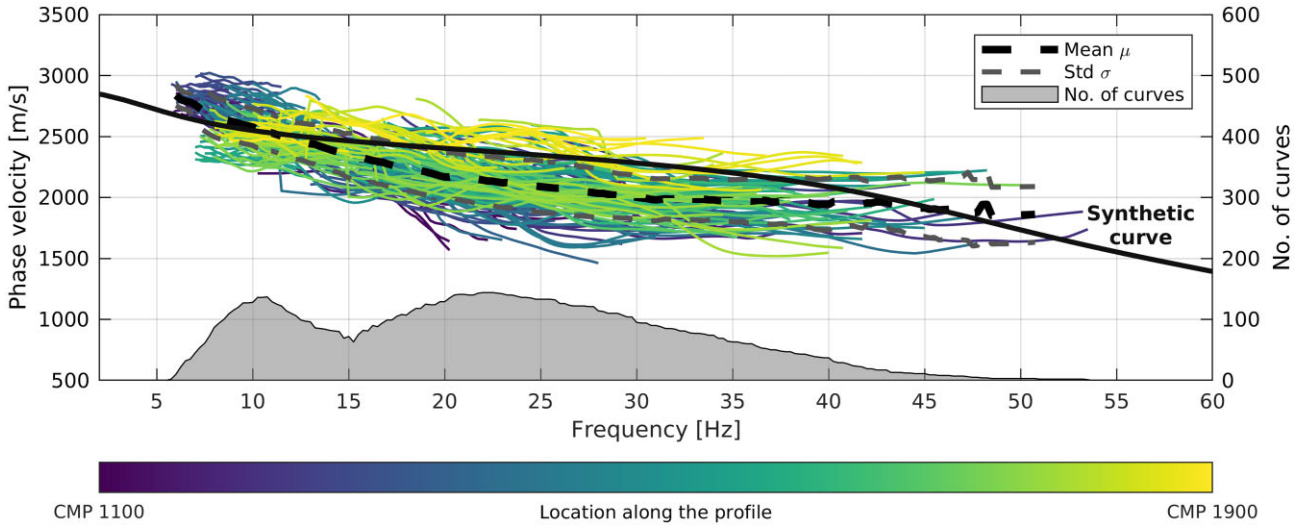


Figure 14. Merged (passive and active) dispersion curves along the profile with the synthetic fundamental mode dispersion curve obtained with a velocity model in Table 1 and a calculated mean and standard deviation. The right *y*-axis corresponds to the number of dispersion curves with a particular frequency (grey area). The colour scale corresponds to the position along the line. Note a longer frequency axis than in Fig. 7.

velocities of the hardrock and the low-frequency content of the ambient noise recorded with broadband receivers (down to 1.25 Hz). Extending the array length would allow for extracting even longer wavelengths (and reaching greater depths) but with a loss of horizontal resolution, as discussed before. On the other hand, we could not extract wavelengths shorter than 150 m due to the low-frequency content, which inhibited us from investigating the first 50 m to 75 m of the subsurface. Thus, the resulting model was not credible shallower than 75 m depth, contrary to active source studies (e.g. Papadopoulou *et al.* 2023), in which this interval was surveyed with high confidence.

By complementing our results with the active source surface-wave analysis, we could image the shallowest 75 m of the subsurface, filling the gaps in the ambient noise section. We resolved the sediment layer with a thickness of less than 20 m, which agrees with the available soil depth model (SGU 2014). Apart from that, the velocity distribution from the ambient noise (Fig. 9) is consistent with the one from merged broadband dispersion curves (Fig. 16) and displayed the same local features, such as two low-velocity zones (around CMP 1500 to 1600 and 1720 to 1780) and high-velocity features at both ends of the profile. Additionally, the velocity variations are located at the positions where we observed scattering in the active source shot gathers.

Thanks to resorting the data to common midpoint gathers, we ensured that, independently from the assumed source-array offset and array length, the used traces are related to this specific point. It allowed us to freely modify the array geometries when needed to avoid disruptive features, such as the arrivals in Fig. 5(b). It also diminished the effect of single noisy virtual shot gathers (e.g. water streams contaminated gathers) thanks to using different

Downloaded from https://academic.oup.com/gji/article/240/1/571/7875257 by Witwatersrand Health Sciences Library user on 08 August 2025

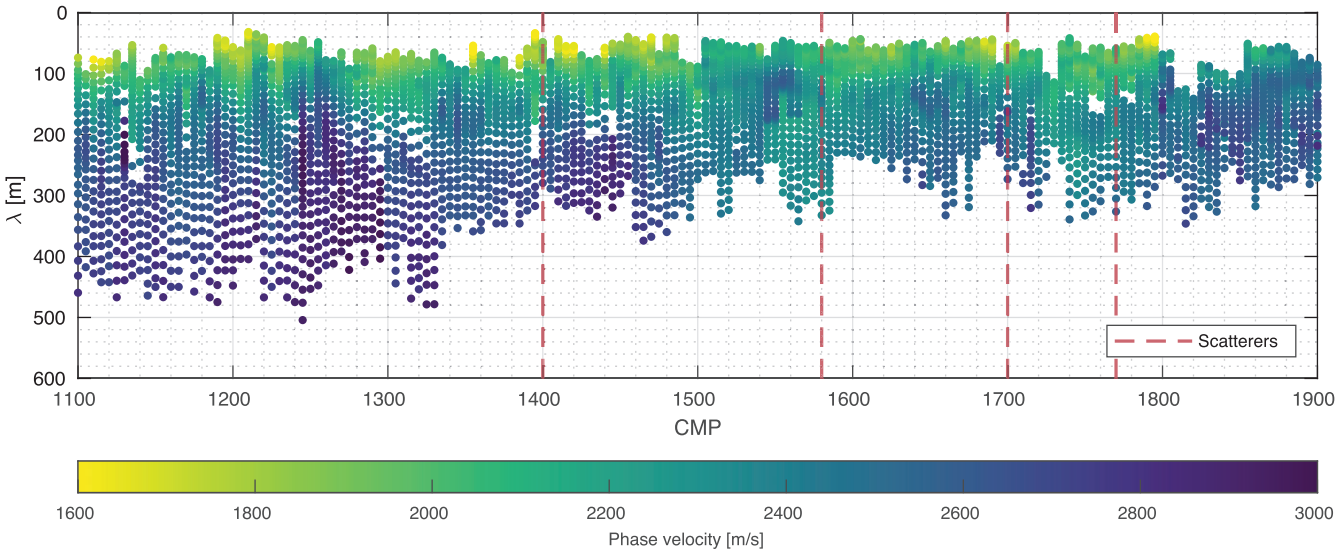


Figure 15. A pseudo-section of merged (passive and active) fundamental mode dispersion curves along the profile with phase velocity colour scaling. The vertical dashed lines present the position of the scatterers observed in the active data (Fig. 3).

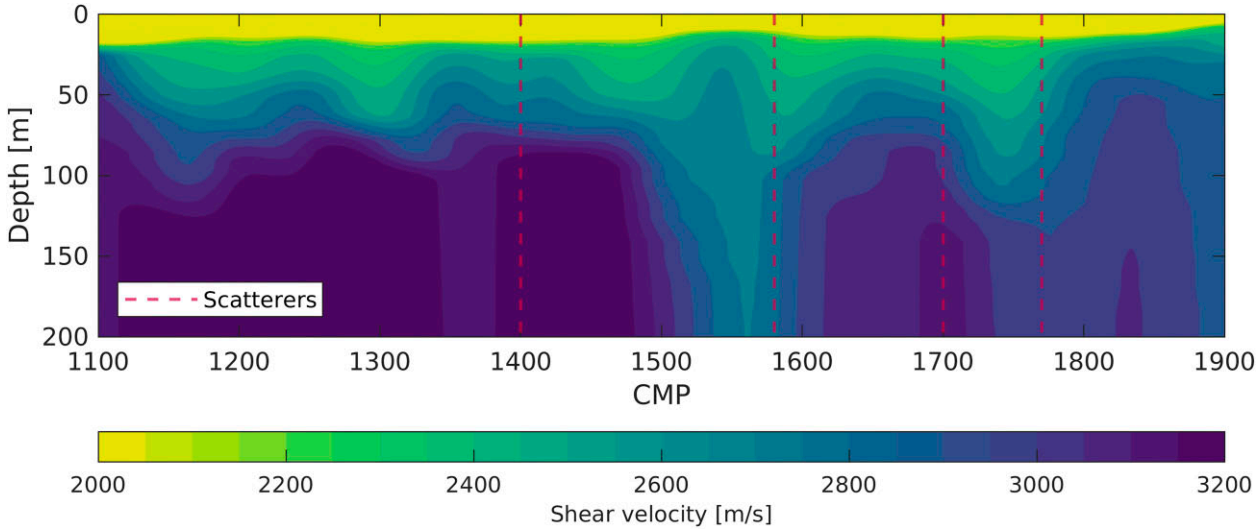


Figure 16. A smoothed merged data (passive and active) 2-D shear-wave velocity section constructed from 1-D models for every fifth CMP. The vertical dashed lines present the position of the scatterers observed in the active data (Fig. 3). Colour scale limits were clipped for a better comparison with other data sets.

Table 2. Comparison of parameters and characteristics for surface-wave analysis of different data sets: passive, active-source and merged.

	Passsive	Active	Merged
Point spacing (m)	12.5	12.5	12.5
Array lengths (m)	200–600	125–500	–
Avg. array length (m)	400	315	–
Source-array offsets (m)	50–500	100	–
Avg. source-array offset (m)	225	160	–
DC frequency range (Hz)	6–16	10–50	6–50
DC phase vel. range (m s−1)	2150–3000	1500–2850	1500–3000
DC wavelength range (m)	125–500	32–250	32–500
Min. resolvable depth λ/3 (m)	40	10	10
Max. resolvable depth λ/2 (m)	250	125	250

Downloaded from https://academic.oup.com/gji/article/240/1/571/7875257 by Witwatersrand Health Sciences Library user on 08 August 2025

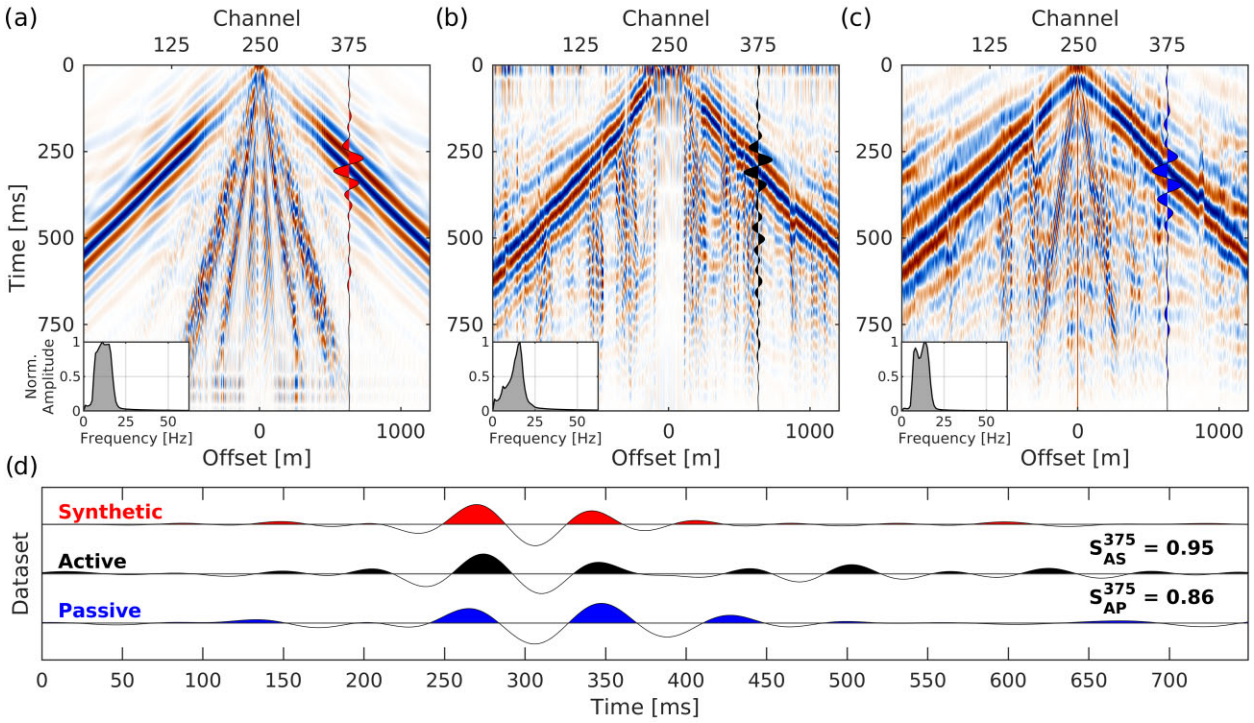


Figure 17. Comparison of the seismic signals in three data sets (shot position 1251). All gathers were bandpass filtered from 6 to 16 Hz. The coloured traces (channel 375) mark the trace used for semblance calculation. (a) Synthetic, generated based on the model in Table 1. (b) Active source data. (c) Passive-retrieved data. (d) Comparison of channels 375 of each gather with calculated semblance: S^{375}_{AS} presents semblance for active and synthetic traces, and S^{375}_{AP} for active and passive traces.

source–receiver combinations. Additionally, it allowed for merging the passive and active dispersion curves regardless of the length of the arrays.

The used linear receiver geometry is suboptimal for ambient noise experiments (Foti *et al.* 2007; Park *et al.* 2007). More suitable geometries, ensuring an omnidirectional array response resolution, are for example an L-shape, a circular pattern (Foti *et al.* 2018) or a pseudo-2-D (Liu *et al.* 2020). In our study, despite the linear geometry, we were able to retrieve the medium's response due to a favourable noise distribution (Fig. 4a), with the seismic noise most likely originating from the rail road and the national road located at the end of the profile. Moreover, the slight line crookedness might have increased the resolution of the array response (e.g. Cheng *et al.* 2023, fig. 14), similarly to a pseudo-2-D array proposed by Liu *et al.* (2020). In case of a disadvantageous source distribution, one could support the investigation with beamforming (Le Feuvre *et al.* 2015; Cheng *et al.* 2016; Foti *et al.* 2018; Liu *et al.* 2020) or correct the phase velocity measurements (Pang *et al.* 2023).

During the processing, we stacked 32 hourly CCFs with a uniform weight, but we observed that not every CCF contributed constructively to the retrieved signal. A weighted cross-correlogram stack could provide a better quality of the retrieved signal. For instance, stacking with implementing coherence-based weights, as suggested by Schimmel *et al.* (2010) or Cheng *et al.* (2015), would enhance the coherent CCF influence on the stack.

In this study, we used nighttime ambient noise for cross-correlation because we observed disrupting arrivals in the daytime data, inhibiting further analysis. However, the daytime data preserved energy also in a higher frequency band than the nighttime data (up to 25 Hz). These disruptions can be overcome either by using a different MASW source-array geometry or in processing (beamforming, muting, etc.). Using the daytime data with a broader frequency range would allow for extracting shorter wavelengths, improving the resolution in the shallow subsurface. It will be considered in future studies.

The disruptive artefact observed in CCFs, marked with black arrows in Figs 5(a) and (b), is of unknown origin. It has a broad frequency range (2 to 50 Hz) and an impulsive nature. Based on the noise distribution plot, we expect the energy to come from the direction of a few buildings within a distance of a few hundred meters towards the southwest. We interpret it as a cultural noise (following Schwardt *et al.* 2022), and we resolved for it by modifying the source-array geometry and top-muting. More on this in Section 3.2.2. Other cross-correlation noise, such as the noisy channels (75, 150, 180, 360 and 430) mentioned in Section 3.2.1 originate from the water flowing in water streams and brooks. We lessened its impact by muting around the true surface-wave arrival, and further through CMP sorting, involving various combinations of sources and receivers. Eventually, the noise did not affect the surface-wave analysis because of the high-data redundancy in the array method (Park *et al.* 1999).

5.2 Versatility and mineral exploration

The possible workflow improvements considered before, such as beamforming, weighted stacking, or utilizing daytime data, could enhance the quality and resolution of the results. However, we argue that the value of our work comes from its versatility. The data were acquired primarily for an active source study and then analysed using conventional processing and well-established methods.

Downloaded from https://academic.oup.com/gji/article/240/1/571/7875257 by Witwatersrand Health Sciences Library user on 08 August 2025

It is thus easier to reproduce and apply in different exploration settings.

A sedimentary (soft-rock) environment is characterized by sedimentary layers of relatively lower phase velocities of the medium, often increasing with depth due to compression. Hence, the wavelengths of the propagating surface waves are relatively shorter and the investigation depth is shallower. However, shorter wavelengths require shorter recording arrays, which allow for a higher lateral resolution (Park & Miller 2008) and improve signal-to-noise ratio (Socco & Strobbia 2004). In a soft-rock environment, to achieve similar depths of investigation as at a stiff site, lower frequencies are required proportionally (Foti *et al.* 2018). In addition, ambient vibrations at soft sites propagate with higher amplitudes (Pileggi *et al.* 2011), increasing the chance of retrieving surface waves from cross-correlations. Thus, ambient noise methods in a soft-rock environment would have a limited investigation depth but would benefit from a higher lateral resolution and easier signal retrieval from the ambient recordings.

Prospecting in a sedimentary environment would particularly benefit from incorporating passive seismic data, which typically allows to extract dispersion curves in a lower frequency range than in active-source experiments (e.g. Foti *et al.* 2007; Park *et al.* 2007). However, when using it as a standalone prospecting method, one would risk misinterpreting the higher depths due to velocity variations in the shallow layers beyond the resolution of the shortest recoverable wavelength. *A priori* information about the shallow subsurface should be incorporated in the inversion scheme as a fixed layer (Socco & Strobbia 2004). Therefore, when possible, one should aim at recording both passive and active data at soft sites or consider other approaches to include broader bandwidths.

In a hardrock environment, the need for *a priori* information about the shallow subsurface can be relaxed due to the small thickness of the soft layer and the crystalline basement's relative homogeneity. In this example, complimenting the passive seismic investigation with an active source study improved the resolution at shallow depths, but did not change the results at depths greater than 75 m. Thus, we argue that harnessing the ambient noise for subsurface characterization can be sufficient if the aim is to detect lateral variations at a significant depth and the medium above is either well-characterized from previous studies or presents marginal vertical heterogeneity. Moreover, the identified features are present in the active source section but are less apparent, proving the value of using merged data sets when investigating greater depths.

Surface-wave analysis in stiff sites requires some considerations in data acquisition and processing. The higher phase velocities and wavelengths, although allowing for a deeper investigation, require longer recording arrays and compromise the later resolution. Related implications were discussed in Section 3.2.2 considering wavenumber limits. Furthermore, Pileggi *et al.* (2011) exemplify that the dominant frequency of the surface wave increases with a thinning soft overburden. To ensure the retrieval of surface waves below the resonant frequencies of the medium, relatively strong ambient vibrations are necessary. However, stiff sites (characterized by a lower Poisson ratio), are known to have lower attenuation, allowing the use of more distant sources in passive seismic experiments (Socco & Strobbia 2004).

Casto *et al.* (2009) showed that to obtain unbiased shear-wave velocity in stiff sites, one needs to narrow the Poisson ratio range in the inversion. In our study, we limited it from 0.1 to 0.35, following the estimates of Maries *et al.* (2017). On sites without prior knowledge of the Poisson ratio, it should be tested within a reasonable range of values.

Mineral deposits rarely occur in sedimentary basins and their exploration is related to hardrock geology (Salisbury *et al.* 2003). Additionally, Eaton *et al.* (2003) and Salisbury *et al.* (2003) show that ores tend to have higher shear-wave velocities than their host rocks. This brings importance to surface-wave studies, as the surface-wave velocity depends primarily on the shear-wave velocity (Socco & Strobbia 2004). Hence, if given an appropriate depth and dimensions within the resolution limits, mineralized bodies can cause a surface-wave anomaly. Because of that, we argue that surface-wave methods should be included in a pool of mineral exploration methods, not only thanks to their ability to detect geological contacts and shear zones but also due to their sensitivity to mineralization.

5.3 Geological interpretation

We use the section presented in Fig. 16, obtained from both passive and active measurements, to provide the geological interpretation. The resulting 2-D shear-wave velocity section presents the subsurface features to depths of ca. 200 m, complementing the shallow depth active source surface-wave studies (e.g. Papadopoulou *et al.* 2019), and deep-targeting reflection seismic studies (e.g. Markovic *et al.* 2019; Pertuz *et al.* 2021; Gyger *et al.* 2023). The section does not reach the main mineralization horizon due to its greater depth (more than 400 m) but aids in identifying shallower features, which may yield potential for further exploration of the area.

The shallow low-velocity layer corresponds to the sediments, mostly glacial tills and sands (Fig. 1d). The colour scale in Fig. 16 was clipped from 2000 m s^{-1}, but the shear-wave velocity values reach down to 1500 m s^{-1}. The thickness of the sediment cover does not exceed 20 m, which agrees with the model of the Geological Survey of Sweden (SGU 2014). The darker colours presenting higher velocities correspond to the crystalline basement (Fig. 1b). To interpret the section in a bigger context, we overlay it on the reflection seismic section of Pertuz *et al.* (2021), and present together with the bedrock geology (SGU 1988, 2018a) and airborne residual magnetic anomaly information (Fig. 18).

The extent of the intrusive metagranitoid had been interpolated from distant outcrops and large-scale magnetic data and is not accurate in a local scale (SGU 1988). However, the marked intrusive-metavolcanic contact corresponds to the high-to-low lateral velocity variation in our shear-wave section (left of the D1 polygon in Fig. 18), validating the bedrock geology map. Thus, we interpret the high-velocity zone, spanning from the beginning of the profile to the D1 polygon in Fig. 18, as an intrusive metagranitoid, and identify the intrusive-metavolcanic contact at CMP 1500. Confirming the extent of the metavolcanic layer is important in the mineral prospecting context, as it was reported to host iron deposits (Geijer & Magnusson 1944; Magnusson 1970).

The shallow reflectors in the reflection section appear below the high-velocity anomaly and neighbour the low-velocity zone (polygon D1 in Fig. 18). Some of them can be projected to the surface near the observed scatterer. With a dip concordant to the main mineralization, high reflectivity and a sharp shear-wave velocity contrast, these events can bring more information about the intrusive-metavolcanic contact and related deformations.

The low shear-wave velocity zone at the end of the profile (polygon D2 in Fig. 18) appears in the vicinity of the previously documented fault (SGU 1988) and observed wave scattering. It was noted before (e.g. Hloušek *et al.* 2022, event C_0) and discussed to be either a fault or a reflector. Based on the observed shear-wave

Downloaded from https://academic.oup.com/gji/article/240/1/571/7875257 by Witwatersrand Health Sciences Library user on 08 August 2025

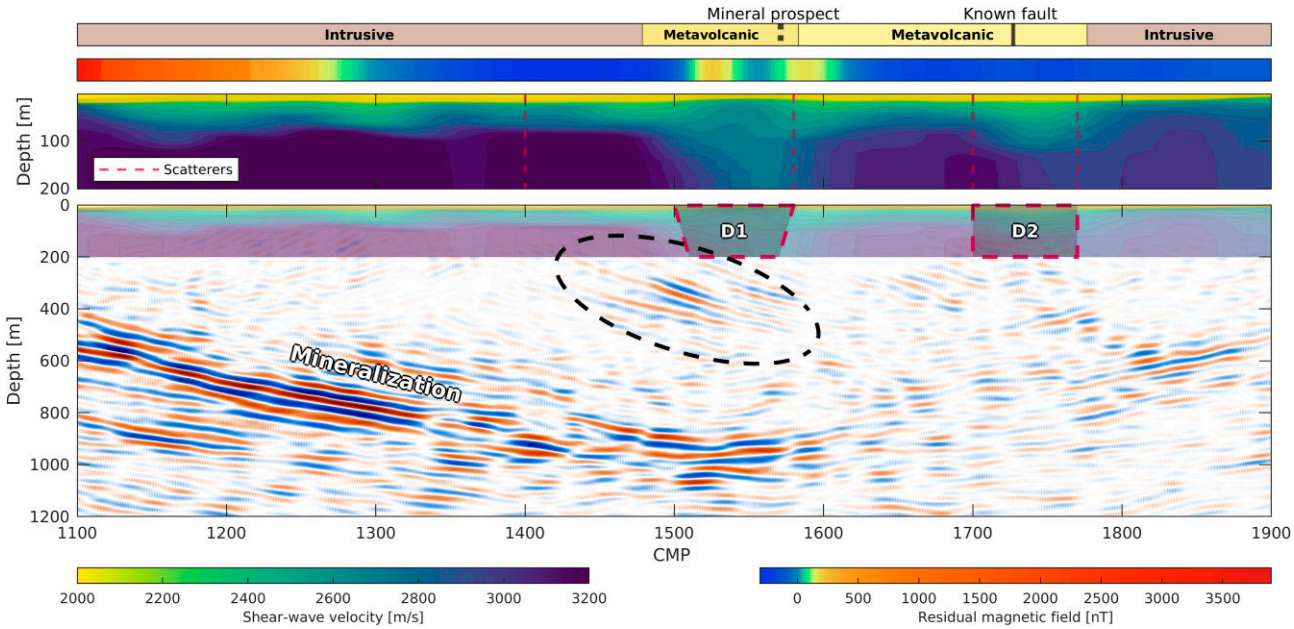


Figure 18. Interpretation of the results using the following panels (top to bottom): surface geology data (SGU 1988), airborne residual magnetic field measurements, shear-velocity section from Fig. 16 with marked scatterers and the same section overlaid (with transparency) on the migrated stacked reflection seismic section (modified after Pertuz *et al.* 2021). The black ellipse indicates the shallow reflections concordant with the high-shear-velocity anomaly. D1 and D2 mark interpreted deformation zones. The deeper event is the main iron-oxide mineralization (Pertuz *et al.* 2021).

velocity anomaly, we argue that this event is a deformation from the known fault and possibly a metavolcanic-intrusive contact, which agrees with the bedrock geology map (Fig. 1b).

The anomalous zone in the middle of the profile (polygon D1 in Fig. 18), was also observed in the study of Papadopoulou *et al.* (2023), which identified a shallow (up to 40 m) low-velocity zone. Moreover, it is present in the tomography and full waveform inversion results of Singh *et al.* (2022). A fracture zone of north–south strike (parallel to the profile) was suggested in this location on a surface geology map by SGU (1988) based on a morphological lineament. Thus, we interpret the D1 polygon as a fracture zone in metavolcanic rocks, with lithological contact between metavolcanic rocks of different compositions proven with wave scattering. A lateral velocity change at CMP 1560 suggests a more complex geology, with either an imprint of a fracture zone, a lithological contact, a presence of thin skarn layers, or a combination of the above. The location is additionally characterized by an elongated high-magnetic anomaly (Fig. 1c). With a former mineral prospect identified in the area, we suggest that this zone contains iron-oxide skarns, yielding a mineral prospecting potential. Other interpretations are also possible and would require further targeted investigation.

Apart from the sediment cover, the geological features are interpretable in both the passive seismic section and the merged data set section (Fig. 9 and Fig. 16, respectively), despite no credibility in the shallowest 75 m of the passive seismic profile. Thus, complementing the passive seismic investigation with an active source study improves the results, but is not required for an overall characterization of rock formations at depth. However, as already discussed, this is valid in hardrock conditions, where the sediment thickness is low, and the vertical rock heterogeneity is marginal.

6 CONCLUSIONS

We have provided a comprehensive surface-wave analysis in a hardrock environment using a conventional reflection seismic acquisition geometry with a nearly linear 2400 m long profile, contextualizing our findings for mineral exploration. The final shear-wave velocity section, obtained by merging dispersion curves from both ambient noise and active source studies, effectively characterized fault zones, confirmed important geological contacts and layer extents and offered new insights into the geological setting. Notably, the shear-wave velocity section from only the ambient noise data was sufficient for an overall geological interpretation, despite lower resolution in the shallow subsurface, and the interpreted features were more apparent than in the active source section.

We have utilized well-known geophysical methods to process and analyse the ambient noise data, such as the ambient noise seismic interferometry and multichannel analysis of surface waves. Reaching moderate depths of several hundred meters, this approach bridges the gap between shallow subsurface and deep-targeting studies. Our work contributes to the general understanding of the geological framework in the mining area of Blötberget, confirms previous findings, and initiates a discussion about other potential mineralization prospects. This suggests that the ambient noise surface-wave analysis can be successfully applied to mineral exploration in hardrock environments as a supplementary method to active source reflection seismic experiments, a validation tool for other geophysical methods, or a standalone prospecting tool for initial surveys.

In particular, we show the application of linear arrays for seismic interferometry and surface-wave analysis methods for prospecting in a hardrock environment. Contrary to a 3-D surface-wave tomography approach, this study highlights the potential of using ambient noise seismic interferometry with cost-effective 2-D geometry to

Downloaded from https://academic.oup.com/gji/article/240/1/571/7875257 by Witwatersrand Health Sciences Library user on 08 August 2025

characterize the subsurface. We argue that this versatile method can also be used with pseudo-2-D and 3-D setups.

ACKNOWLEDGMENTS

We sincerely thank Editor Prof. Huajian Yao and the reviewers, Deyan Draganov and an anonymous reviewer, for their valuable and constructive comments that helped improve our manuscript. The experiment was conducted within the framework of ERA-MIN3 FUTURE, a European-South African project aimed at developing innovative methods for mining exploration (VINNOVA grant no. 2022-00073). We are grateful for the support. We acknowledge Wathelet *et al.* (2020), the creators of Geopsy, an open-source tool for ambient vibrations processing, which we used in our work. We also thank van den Ende & Ampuero (2021) for publishing their codes for MUSIC beamforming, and the reflection seismology group from Uppsala University, particularly Prof. Christopher Juhlin for suggesting the weathered bedrock hypothesis and Lea Gyger for providing the first break traveltime picks.

DATA AVAILABILITY

Research data will be available after the data set potential has been explored by the project collaborators. Currently, there is a 3-yr embargo on the data. For further instructions, contact Prof. Alireza Malehmir at alireza.malehmir@geo.uu.se.

REFERENCES

Alcalde, J., Carbonell, R., Pospiech, S., Gil, A., Bullock, L.A. & Tornos, F., 2022. Preface: State of the art in mineral exploration, *Solid Earth,* **13**(7), 1161–1168.

Ali, S.H. *et al.*, 2017. Mineral supply for sustainable development requires resource governance, *Nature,* **543**(7645), 367–372.

Allen, R.L., Lundstrom, I., Ripa, M. & Christofferson, H., 1996. Facies analysis of a 1.9 ga, continental margin, back-arc, felsic caldera province with diverse zn-pb-ag-(cu-au) sulfide and fe oxide deposits, bergslagen region, sweden, *Econ. Geol.,* **91**(6), 979–1008.

Bakulin, A. & Calvert, R., 2006. The virtual source method: Theory and case study, *Geophysics,* **71**(4), SI139–SI150.

Balestrini, F., Draganov, D., Malehmir, A., Marsden, P. & Ghose, R., 2019. Improved target illumination at ludvika mines of sweden through seismic-interferometric surface-wave suppression, *Geophys. Prospect.,* **68**(1), 200–213.

Bensen, G.D., Ritzwoller, M.H., Barmin, M.P., Levshin, A.L., Lin, F., Moschetti, M.P., Shapiro, N.M. & Yang, Y., 2007. Processing seismic ambient noise data to obtain reliable broadband surface wave dispersion measurements, *J. geophys. Int.,* **169**(3), 1239–1260.

Campillo, M. & Paul, A., 2003. Long-range correlations in the diffuse seismic coda, *Science,* **299**(5606), 547–549.

Casto, D.W., Luke, B., Calderón-Macías, C. & Kaufmann, R., 2009. Interpreting surface-wave data for a site with shallow bedrock, *J. Environ. Eng. Geophys.,* **14**(3), 115–127.

Chamarczuk, M., Malinowski, M., Draganov, D., Koivisto, E., Heinonen, S. & Rötsä, S., 2022. Reflection imaging of complex geology in a crystalline environment using virtual-source seismology: case study from the kylylahti polymetallic mine, finland, *Solid Earth,* **13**(3), 705–723.

Chen, G., Cheng, Q., Luo, Y., Yang, Y., Xu, H. & Deng, X., 2021. Seismic imaging of the caosiyao giant porphyry molybdenum deposit using ambient noise tomography, *Geophysics,* **86**(6), B401–B412.

Cheng, F. *et al.*, 2016. Multichannel analysis of passive surface waves based on crosscorrelations, *Geophysics,* **81**(5), EN57–EN66.

Cheng, F., Xia, J. & Xi, C., 2023. Artifacts in high-frequency passive surface wave dispersion imaging: Toward the linear receiver array, *Surv. Geophys.,* **44**(4), 1009–1039.

Cheng, F., Xia, J., Xu, Y., Xu, Z. & Pan, Y., 2015. A new passive seismic method based on seismic interferometry and multichannel analysis of surface waves, *J. Appl. Geophys.,* **117,** 126–135.

Claerbout, J.F., 1968. Synthesis of a layered medium from its acoustic transmission response, *Geophysics,* **33**(2), 264–269.

Colombero, C., Papadopoulou, M., Kauti, T., Skyttä, P., Koivisto, E., Savolainen, M. & Socco, L.V., 2022. Surface-wave tomography for mineral exploration: a successful combination of passive and active data (siilinjärvi phosphorus mine, finland), *Solid Earth,* **13**(2), 417–429.

Curtis, A., Gerstoft, P., Sato, H., Snieder, R. & Wapenaar, K., 2006. Seismic interferometry—turning noise into signal, *Leading Edge,* **25**(9), 1082–1092.

Da Col, F., Papadopoulou, M., Koivisto, E., Sito, Ł., Savolainen, M. & Socco, L.V., 2019. Application of surface-wave tomography to mineral exploration: a case study from siilinjärvi, finland, *Geophys. Prospect.,* **68**(1), 254–269.

dal Moro, G., 2015. *Surface Wave Analysis for Near Surface Applications,* Elsevier.

Deng, B., Li, J., Liu, J., Shen, C., Suwen, J. & Chen, Q.-F., 2022. The extended range phase shift method for broadband surface wave dispersion measurement from ambient noise and its application in ore deposit characterization, *Geophysics,* **87**(3), JM29–JM40.

Draganov, D., Campman, X., Thorbecke, J., Verdel, A. & Wapenaar, K., 2013. Seismic exploration-scale velocities and structure from ambient seismic noise (< 1 hz), *J. Geophys. Res.: Solid Earth,* **118**(8), 4345–4360.

Draganov, D., Wapenaar, K., Mulder, W., Singer, J. & Verdel, A., 2007. Retrieval of reflections from seismic background-noise measurements, *Geophys. Res. Lett.,* **34**(4), doi:10.1029/2006GL028735.

Eaton, D., B., Milkereit & M., Salisbury, 2003. Hardrock Seismic Exploration: Mature technologies adapted to new exploration targets, *Hardrock Seismic Exploration,* vol. **10,** i–6, eds, Eaton D., Milkereit B. & Salisbury M., Society of Exploration Geophysicists.

Foti, S. *et al.*, 2018. Guidelines for the good practice of surface wave analysis: a product of the interpacific project, *Bull. Earthq. Eng.,* **16**(6), 2367–2420.

Foti, S., Comina, C. & Boiero, D., 2007. Reliability of combined active and passive surface wave methods, *Riv. Ital. Geotec.,* **41**(2), 39–47.

Foti, S., Lai, C., Rix, G.J. & Strobbia, C., 2014. *Surface Wave Methods for near-Surface Site Characterization,* Taylor & Francis Group, 1–487.

Geijer, P. & Magnusson, N., 1944. *De Mellansvenska Järnmalmernas Geologi,* p. 654, eds, Geijer P. & Magnusson N., Sveriges geologiska undersökning, Ca 35.

Gerstoft, P., Sabra, K.G., Roux, P., Kuperman, W.A. & Fehler, M.C., 2006. Green's functions extraction and surface-wave tomography from microseisms in southern california, *Geophysics,* **71**(4), SI23–SI31.

Goodenough, K. *et al.*, 2016. Europe's rare earth element resource potential: An overview of ree metallogenetic provinces and their geodynamic setting, *Ore Geol. Rev.,* **72,** 838–856.

Gyger, L. *et al.*, 2023. Broadband seismic acquisition and processing in hardrock environment: a case study from blötberget, sweden, in *NSG2023 29th European Meeting of Environmental and Engineering Geophysics,* 1–5, European Association of Geoscientists & Engineers.

Gyger, L., Malehmir, A., Manzi, M., Vivin, L., Lepine, J., Kaslilar, A. & Marsden, P., 2022. Simultaneous borehole-surface distributed acoustic sensing for deep iron-oxide deposit targeting in blötberget, Sweden, in *Proceedings of SAGA Biennial Conference & Exhibition*.

Halliday, D. & Curtis, A., 2008. Seismic interferometry, surface waves and source distribution, *J. geophys. Int.,* **175**(3), 1067–1087.

Halliday, D., Curtis, A. & Kragh, E., 2008. Seismic surface waves in a suburban environment: Active and passive interferometric methods, *Leading Edge,* **27**(2), 210–218.

Downloaded from https://academic.oup.com/gji/article/240/1/571/7875257 by Witwatersrand Health Sciences Library user on 08 August 2025

Hloušek, F. *et al.*, 2022. Three-dimensional reflection seismic imaging of the iron oxide deposits in the ludvika mining area, sweden, using fresnel volume migration, *Solid Earth,* **13**(5), 917–934.

Högdahl, K., Jonsson, E. & Malehmir, A., 2020. Magmatic and metamorphic ages of the host rocks to apatite-iron oxide deposits in the Grängesberg-Blötberget area, Bergslagen, Sweden, in *NGF Abstracts and Proceedings 1,* p. 95, eds, Nakrem, H. A. & Husås, A. M., Norway.

Ivanov, J., Miller, R. & Peterie, S., 2016. Detecting and delineating voids and mines using surface-wave methods in galena, kansas, in *SEG Technical Program Expanded Abstracts 2016,* 2344–2350, eds, Sickling, C. & Ferguson, J., Society of Exploration Geophysicists.

Jonsson, E., Troll, V.R., Högdahl, K., Harris, C., Weis, F., Nilsson, K.P. & Skelton, A., 2013. Magmatic origin of giant 'kiruna-type' apatite-iron-oxide ores in central sweden, *Sci. Rep.,* **3**(1), 1644, doi:10.1038/srep01644.

Kaslilar, A., Wilczynski, Z., Markovic, M., Marsden, P., Manzi, M. & Malehmir, A., 2022. A prefeasibility study for passive seismic imaging in hard rock environment, in *NSG2022 4th Conference on Geophysics for Mineral Exploration and Mining,* European Association of Geoscientists & Engineers.

Le Feuvre, M., Joubert, A., Leparoux, D. & Côte, P., 2015. Passive multichannel analysis of surface waves with cross-correlations and beamforming. application to a sea dike, *J. Appl. Geophys.,* **114,** 36–51.

Li, M., Fang, H. & Gao, R., 2023. Ambient noise tomography using a nodal seismic array reveals evidence for igneous intrusion contributed to ore deposits in south china, *Seismol. Res. Lett.,* **94**(6), 2765–2774.

Liu, Q., Feng, X., Liu, C., Zhang, M., Tian, Y. & Hou, H., 2022. Metallic mineral exploration by using ambient noise tomography in ashele copper mine, xinjiang, china, *Geophysics,* **87**(3), B221–B231.

Liu, Y., Xia, J., Cheng, F., Xi, C., Shen, C. & Zhou, C., 2020. Pseudo-linear-array analysis of passive surface waves based on beamforming, *J. geophys. Int.,* **221**(1), 640–650.

Louie, J.N., 2001. Faster, better: Shear-wave velocity to 100 meters depth from refraction microtremor arrays, *Bull. seism. Soc. Am.,* **91**(2), 347–364.

Magnusson, N.H., 1970. *The Origin of the Iron Ores in Central Sweden and the History of their Alterations. Part I: Text., Serie C, Avhandlingar Och Uppsatser,* 643, Sveriges Geologiska Undersökning,

Malehmir, A. *et al.*, 2021. Sparse 3d reflection seismic survey for deep-targeting iron oxide deposits and their host rocks, ludvika mines, sweden, *Solid Earth,* **12**(2), 483–502.

Malehmir, A., Durrheim, R., Bellefleur, G., Urosevic, M., Juhlin, C., White, D.J., Milkereit, B. & Campbell, G., 2012. Seismic methods in mineral exploration and mine planning: A general overview of past and present case histories and a look into the future, *Geophysics,* **77**(5), WC173–WC190.

Malehmir, A., Gisselø, P., Socco, V., Carvalho, J., Marsden, P., Verboon, A.O. & Loska, M., 2020. Smart exploration inspires innovative geophysical solutions for mineral exploration in europe, *First Break,* **38**(12), 51–56.

Malehmir, A., Maries, G., Bäckström, E., Schön, M. & Marsden, P., 2017. Developing cost-effective seismic mineral exploration methods using a landstreamer and a drophammer, *Sci. Rep.,* **7**(1), doi:10.1038/s41598-017-10451-6.

Malehmir, A., Markovic, M., Papadopoulou, M. & Marsden, P., 2023. Establishment of a hardrock seismic test site in central Sweden, in *Proceedings of KEGS PDAC Symposium 2023, KEGS PDAC Symposium 2023*.

Maries, G., Malehmir, A., Bäckström, E., Schön, M. & Marsden, P., 2017. Downhole physical property logging for iron-oxide exploration, rock quality, and mining: An example from central sweden, *Ore Geol. Rev.,* **90,** 1–13.

Markovic, M., Malehmir, A. & Manzi, M., 2023. Establishing a baseline multi-component reflection seismic imaging of iron-oxide deposits at ludvika mines, central Sweden, in *84th EAGE Annual Conference & Exhibition,* 1–5 European Association of Geoscientists & Engineers.

Markovic, M., Maries, G., Malehmir, A., von Ketelhodt, J., Bäckström, E., Schön, M. & Marsden, P., 2019. Deep reflection seismic imaging of iron-oxide deposits in the ludvika mining area of central sweden, *Geophys. Prospect.,* **68**(1), 7–23.

McBride, J.H., Nelson, S.T., Park, C.B., Wolfe, E.E., Tingey, D.G. & Rey, K.A., 2019. Ocean waves as a passive masw source, *J. Appl. Geophys.,* **171,** 103 860, doi:10.1016/j.jappgeo.2019.103860.

Nordic Iron Ore, 2011. *Ludvika Mines Preliminary Economic Assessment. Final Report. rev. 3:1-74, Techreport,* Nordic Iron Ore, 1–8

Olivier, G. *et al.*, 2024. Ambient noise tomography of an iron-oxide copper–gold (iocg) deposit under thick cover, *Exploration Geophysics,* **55**(6), 667–677.

Pan, Y., Xia, J., Xu, Y., Xu, Z., Cheng, F., Xu, H. & Gao, L., 2016. Delineating shallow s-wave velocity structure using multiple ambient-noise surface-wave methods: An example from western junggar, china, *Bull. seism. Soc. Am.,* **106**(2), 327–336.

Pang, J., Xia, J., Cheng, F., Zhou, C., Chen, X., Shen, C., Xing, H. & Chang, X., 2023. Surface wave dispersion measurement with polarization analysis using multicomponent seismic noise recorded by a 1-d linear array, *Surv. Geophys.,* **44**(6), 1863–1895.

Papadopoulou, M., 2021. *Surface-wave Methods for Mineral Exploration, PhD Thesis,* Politecnico di Torino.

Papadopoulou, M., Brodic, B., Koivisto, E., Kaleshova, A., Savolainen, M., Marsden, P. & Socco, L.V., 2023. High-resolution static corrections derived from surface-wave tomography: Application to mineral exploration, *Geophysics,* **88**(6), B317–B328.

Papadopoulou, M., Da Col, F., Mi, B., Bäckström, E., Marsden, P., Brodic, B., Malehmir, A. & Socco, L.V., 2019. Surface-wave analysis for static corrections in mineral exploration: A case study from central sweden, *Geophys. Prospect.,* **68**(1), 214–231.

Park, C.B. & Miller, R.D., 2008. Roadside passive multichannel analysis of surface waves (masw), *J. Environ. Eng. Geophys.,* **13**(1), 1–11.

Park, C.B., Miller, R.D. & Xia, J., 1999. Multichannel analysis of surface waves, *Geophysics,* **64**(3), 800–808.

Park, C.B., Miller, R.D., Xia, J. & Ivanov, J., 2007. Multichannel analysis of surface waves (masw)—active and passive methods, *Leading Edge,* **26**(1), 60–64.

Pertuz, T., Malehmir, A., Bos, J., Brodic, B., Ding, Y., de Kunder, R. & Marsden, P., 2021. Broadband seismic source data acquisition and processing to delineate iron oxide deposits in the blötberget mine-central sweden, *Geophys. Prospect.,* **70**(1), 79–94.

Pileggi, D., Rossi, D., Lunedei, E. & Albarello, D., 2011. Seismic characterization of rigid sites in the itaca database by ambient vibration monitoring and geological surveys, *Bull. Earthq. Eng.,* **9**(6), 1839–1854.

Rector, J.W., Pfeiffe, J., Hodges, S., Kingman, J. & Sprott, E., 2015. Tomographic imaging of surface waves: A case study from the phoenix mine, battle mountain, nevada, *Leading Edge,* **34**(11), 1360–1364.

Ripa, M. & Kübler, L., 2003. *Apatite-Bearing Iron Ores in the Bergslagen Region of South-Central Sweden,* **2,** 49–54, ed. Ripa, M., Sveriges geologiska undersökning, Uppsala.

Roux, P., Sabra, K.G., Gerstoft, P., Kuperman, W.A. & Fehler, M.C., 2005. P-waves from cross-correlation of seismic noise, *Geophys. Res. Lett.,* **32**(19), doi:10.1029/2005GL023803.

Ryberg, T., Kirsch, M., Haberland, C., Tolosana-Delgado, R., Viezzoli, A. & Gloaguen, R., 2022. Ambient seismic noise analysis of large-n data for mineral exploration in the central erzgebirge, germany, *Solid Earth,* **13**(3), 519–533.

Ryden, N. & Mooney, M.A., 2009. Analysis of surface waves from the light weight deflectometer, *Soil Dynamics and Earthquake Engineering,* **29**(7), 1134–1142.

Salisbury, M.H., Harvey, C.W. & Matthews, L., 2003. *1. The Acoustic Properties of Ores and Host Rocks in Hardrock Terranes,* pp. 9–19, Eaton, D. W. & Salisbury, M. H., Bernd M., Society of Exploration Geophysicists.

Schimmel, M., Stutzmann, E. & Gallart, J., 2010. Using instantaneous phase coherence for signal extraction from ambient noise data at a local to a global scale: Ambient noise signal extraction, *J. geophys. Int.,* **184**(1), 494–506.

Downloaded from https://academic.oup.com/gji/article/240/1/571/7875257 by Witwatersrand Health Sciences Library user on 08 August 2025

Schwardt, M., Pilger, C., Gaebler, P., Hupe, P. & Ceranna, L., 2022. Natural and anthropogenic sources of seismic, hydroacoustic, and infrasonic waves: Waveforms and spectral characteristics (and their applicability for sensor calibration), *Surveys in Geophysics,* **43**(5), 1265–1361.

SGU, 1988. *Af 158 Berggryndskartan 12f Ludvika sv Med Flygmagnetisk Och Strukturgeologisk Karta, Map,* Sveriges geologiska undersökning, Scale 1:50 000.

SGU, 2014. *Rikstäckande Jorddjupsmodell, SGU-Rapport 2014:14,* 1–14, eds, Daniels, J. & Thunholm, B., Sveriges Geologiska Undersökning.

SGU, 2018a. *Berggrund, Map, Sveriges Geologiska Undersökning,* Scale 1:50 000-1:250 000.

SGU, 2018b. *Jordarter, Map, Sveriges Geologiska Undersökning,* Scale 1:25 000-1:100 000.

SGU, 2022. *Kartering i Området Grängesbergidkerberget–Fältarbeten 2021, SGU-Rapport 2022:03,* eds, Lewerentz, A. & Brolin, C., Sveriges Geologiska Undersökning.

Shapiro, N.M., Campillo, M., Stehly, L. & Ritzwoller, M.H., 2005. High-resolution surface-wave tomography from ambient seismic noise, *Science,* **307**(5715), 1615–1618.

Sherman, C., Rector, J., Dreger, D. & Glaser, S., 2014. Seismic tunnel detection at black diamond mines regional preserve, in *SEG Technical Program Expanded Abstracts 2014,* 2078–2082, ed. Birkelo, B., Society of Exploration Geophysicists.

Singh, B., Malinowski, M., Górszczyk, A., Malehmir, A., Buske, S., Sito, Ł. & Marsden, P., 2022. 3d high-resolution seismic imaging of the iron oxide deposits in ludvika (sweden) using full-waveform inversion and reverse time migration, *Solid Earth,* **13**(6), 1065–1085.

Snieder, R. & Wapenaar, K., 2010. Imaging with ambient noise, *Phys. Today,* **63**(9), 44–49.

Snieder, R., Sheiman, J. & Calvert, R., 2006. Equivalence of the virtual-source method and wave-field deconvolution in seismic interferometry, *Phys. Rev. E,* **73**(6), 066 620.

Socco, L. & Strobbia, C., 2004. Surface-wave method for near-surface characterization: a tutorial, *Near Surf. Geophys.,* **2**(4), 165–185.

Socco, L.V., Foti, S. & Boiero, D., 2010. Surface-wave analysis for building near-surface velocity models—established approaches and new perspectives, *Geophysics,* **75**(5), 75A83–75A102.

Stephens, M.B., 2009. *Synthesis of the Bedrock Geology in the Bergslagen Region, Fennoscandian Shield, South-Central Sweden,* Serie: Sveriges geologiska undersökning. Serie Ba, Översiktskartor med beskrivningar, 0373-2657, ed. Stephens, M.B., Uppsala.

Strobbia, C. & Cassiani, G., 2011. Refraction microtremors: Data analysis and diagnostics of key hypotheses, *Geophysics,* **76**(3), MA11–MA20.

Thorbecke, J.W. & Draganov, D., 2011. Finite-difference modeling experiments for seismic interferometry, *Geophysics,* **76**(6), H1–H18.

van den Ende, M. P.A. & Ampuero, J.-P., 2021. Evaluating seismic beamforming capabilities of distributed acoustic sensing arrays, *Solid Earth,* **12**(4), 915–934.

Wang, K., Qian, J., Zhang, H., Gao, J., Bi, D. & Gu, N., 2022. Seismic imaging of mine tunnels by ambient noise along linear arrays, *J. Appl. Geophys.,* **203,** 104 718.

Wapenaar, K., 2004. Retrieving the elastodynamic green's function of an arbitrary inhomogeneous medium by cross correlation, *Phys. Rev. Lett.,* **93**(25), 254 301.

Wathelet, M., 2005. *Array Recordings of Ambient Vibrations: Surface-Wave Inversion,* Ph.D. thesis, Liège University.

Wathelet, M., 2008. An improved neighborhood algorithm: Parameter conditions and dynamic scaling, *Geophys. Res. Lett.,* **35**(9).

Wathelet, M., Chatelain, J.-L., Cornou, C., Giulio, G.D., Guillier, B., Ohrnberger, M. & Savvaidis, A., 2020. Geopsy: A user-friendly open-source tool set for ambient vibration processing, *Seismol. Res. Lett.,* **91**(3), 1878–1889.

Wilczynski, Z., Kaslilar, A., Malehmir, A., Manzi, M., Vivin, L., Lepine, J. & Valishin, O., 2023. Synthetic, broadband mems, and das comparison - surface-borehole array for surface-wave analysis and mineral exploration., in *84th EAGE Annual Conference & Exhibition,* European Association of Geoscientists & Engineers, 1–5.

Xia, J., Miller, R.D., Park, C.B., Hunter, J.A., Harris, J.B. & Ivanov, J., 2002. Comparing shear-wave velocity profiles inverted from multichannel surface wave with borehole measurements, *Soil Dyn. Earthq. Eng.,* **22**(3), 181–190.

Yao, H., van der Hilst, R.D. & de Hoop, M.V., 2006. Surface-wave array tomography in se tibet from ambient seismic noise and two-station analysis - i. phase velocity maps, *J. geophys. Int.,* **166**(2), 732–744.

Zhang, H., Mi, B., Xi, C., Liu, Y., Guan, B. & Ning, L., 2022. Extraction of surface-wave phase velocities from ambient noise in the presence of local noise sources based on matched-field processing, *J. Appl. Geophys.,* **204,** 104 755.

Zhao, Y., Li, Y.E. & Li, B., 2023. On beamforming of das ambient noise recorded in an urban environment and rayleigh-to-love wave ratio estimation, *J. Geophys. Res.: Solid Earth,* **128**(8), doi:10.1029/2022JB026339.

Zheng, F., Xu, T., Ai, Y., Yang, Y., Zeng, Q., Yu, B., Zhang, W. & Xie, T., 2022. Metallogenic potential of the wulong goldfield, liaodong peninsula, china revealed by high-resolution ambient noise tomography, *Ore Geol. Rev.,* **142,** 104 704.

Downloaded from https://academic.oup.com/gji/article/240/1/571/7875257 by Witwatersrand Health Sciences Library user on 08 August 2025

© The Author(s) 2024. Published by Oxford University Press on behalf of The Royal Astronomical Society. This is an Open Access article distributed under the terms of the Creative Commons Attribution License (https://creativecommons.org/licenses/by/4.0/), which permits unrestricted reuse, distribution, and reproduction in any medium, provided the original work is properly cited.